Food Hydrocolloids 142 (2023) 108851

Contents lists available at ScienceDirect

Food Hydrocolloids

journal homepage: www.elsevier.com/locate/foodhyd

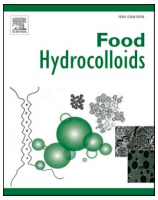

Self-assembly of plant polyphenols-grafted soy proteins to manufacture a highly stable antioxidative Pickering emulsion gel for direct-ink-write 3D printing

Adeleh Mohammadi [a], Peyman Asghartabar Kashi [b], Mahboobeh Kashiri [a], Amirhossein Bagheri [a], Jianshe Chen [c], Rammile Ettelaie [d], Henry Jäger [e,*], Mahdiyar Shahbazi [e,**]

[a] Faculty of Food Science and Technology, Gorgan University of Agricultural Sciences and Natural Resources, Gorgan, Iran
[b] Faculty of Biosystem, College of Agricultural and Natural Resources Tehran University, Tehran, Iran
[c] Food Oral Processing Laboratory, School of Food Science & Biotechnology, Zhejiang Gongshang University, Hangzhou, China
[d] Food Colloids and Bioprocessing Group, School of Food Science and Nutrition, University of Leeds, Leeds, LS2 9JT, UK
[e] Institute of Food Technology, University of Natural Resources and Life Sciences (BOKU), Muthgasse 18, 1190, Vienna, Austria

ARTICLE INFO

Keywords:
Functional food
Plant based cheese
Surface modification
Interfacial adsorbed layers
CLSM
Printability
3D printing
Temporal dominance of sensation

ABSTRACT

The practicable application of 3D printing in the pharmaceutical and food sectors directly relates to the preparation of highly stable bioactive printable inks. Here, three different polyphenols (rosemary polyphenols, thyme polyphenols, and basil polyphenols) were individually grafted onto soy protein isolate through a free-radical grafting method to produce a precursor printable ink to develop 3D printed plant-based cheese. The morphological features, emulsion rheology measurements, quartz crystal microbalance with dissipation monitoring techniques, and interfacial shear rheology were used to monitor emulsification features and interfacial rheology (i.e., adsorption kinetics, viscoelastic features, and interfacial adsorbed layers) of precursor inks. Compared to soy-based ink, polyphenols-grafted soy protein inks developed more stable emulsions against coalescence with finer droplets. Also, the interfacial adsorption properties of protein particles were improved after the grafting process, in which the surface dilatational viscoelastic moduli and interfacial pressure were boosted. The ink formulating by soy protein-*g*-rosemary polyphenols (with greater hydrophobicity) showed a emulsion droplets with smaller size, had a stiffer structure, and stronger surface activity than inks containing soy protein-*g*-thyme or soy protein-*g*-basil polyphenols, which displayed a 3D printed cheese analogue with improved lubrication property, higher creamy sensation and mouth-coating feature. Overall, this work suggests that compatibilization of the plant polyphenols and the soy proteins offers an opportunity for adopting plant-based inks in the 3D printing of advanced materials.

1. Introduction

The emergence of the 3D printing technique is an innovative concept possibly valuable to manufacturing functional 3D structures. The 3D printing via material extrusion of printable inks is also detected as direct-ink-writing (DIW) or robocasting, where the delivery system (like an extruder) precisely deposits the accurate amount of thixotropic and viscoelastic ink over adjustable distances (Corker, Ng, Poole, & García-Tuñón, 2019; Eguiluz, Ferrández-Montero, Yus, Sanchez-Herencia, & Ferrari, 2021; Guo et al., 2023; Mohammadi, Movahhedy, & Khodaygan, 2021; Vadodaria, He, Mills, & Wildman, 2020). Printability of biopolymers-based inks is then a critical parameter to producing well-defined 3D printed products, which is directly influenced by the flow behavior of the inks (Chen, Zhang, Pang, Liu, & Liu, 2021; Elbadawi, Gustaffson, Gaisford, & Basit, 2020; Maldonado-Rosas et al., 2022; Outrequin, Gamonpilas, Siriwatwechakul, & Sreearunothai, 2022; Shahbazi et al., 2021a). Indeed, the capability of ink to extrude from a printer nozzle is associated with its rheological properties

* Corresponding author.
** Corresponding author.
E-mail addresses: henry.jaeger@boku.ac.at (H. Jäger), mahdiyar.shahbazi@boku.ac.at, shahbazim00@yahoo.com (M. Shahbazi).

https://doi.org/10.1016/j.foodhyd.2023.108851
Received 19 March 2023; Received in revised form 26 April 2023; Accepted 2 May 2023
Available online 2 May 2023

including consistency and flow behavior indices, as well as yield stress (Polamaplly et al., 2019; Hu et al., 2022; Nair, Panda, Santhanam, Sant, & Neithalath, 2020; Shahbazi et al., 2021b; Shahbazi & Jäger, 2020). These parameters strongly influence the essential pressure appropriate for actual extrudability, printing accuracy, shape fidelity, and printing precision of printed structures. Alongside this, accurate stability and formation of the printed objects are also essential to engineer a self-supported 3D architecture. The knowledge of the relaxation time, viscoelastic moduli, and extensional features of the inks is therefore pertinent in developing a high-quality 3D object (Riantiningtyas et al., 2021; Shi, Zhang, & Bhandari, 2021; Zeng, Li, Zhu, Chen, & Zheng, 2021).

A versatile and promising processing way for rapid prototyping is the printing of inks as emulsion templating systems (Caulier, Doets, & Noort, 2020; Liu, Xu, Zong, Yu, & Zhang, 2021). As the printing systems often apply a high level of temperature and shearing forces, emulsions are prone to experiencing phase separation during the process. During the 3D printing process, a possible deformation of emulsion-based inks does not allow the 3D printed layers to be effectively deposited and stacked to engineer a well-defined designed shape. As a semi-solid colloidal dispersion, emulsion gels combine the properties of both emulsions and gels, which offer crucial consistency to fabricating complex and highly customized structures. Emulsion gels have a possible application in 3D printing and were stated to show great printability because of the satisfactory flow behavior and physical stability under the extrusion (Andriamiseza, Bordignon, Payré, Vaysse, & Fitremann, 2022; Liu, Song, et al., 2021). The reported outstanding flow behavior of emulsion gels including high viscosity (Du et al., 2022; Qiu et al., 2022), shear thinning feature (Chen, Cao, & Advincula, 2018; Chen et al., 2020), suitable storage modulus (Shahbazi, Jäger, Ettelaie, & Chen, 2021; Wan, Wang, Feng, Chen, & Wang, 2021), good thixotropic behavior (Liu et al., 2019; Shahbazi et al., 2021c), excellent printability (Li et al., 2020; Shahbazi et al., 2022a), outstanding structural recovery (Chen et al., 2018; Sommer et al., 2017), and self-supporting features (Sheikhi, Rafiemanzelat, Ghodsi, Moroni, & Setayeshmehr, 2022; Yuan, Wu, & Fu, 2022) are demonstrated to favor adjustable injectability, smooth extrusion features, printability, printing performance, resolution and shape fidelity, a distinguished 3D matrix, and retained permanent deformation after unloading (Liu & Li, 2017), as well as flavor maintenance of the 3D printing objects (Fahmy et al., 2021).

It has been well established that the functional properties of proteins can be considerably improved by numerous physical, chemical, and enzymatic modification approaches (Shahbazi & Jäger, 2020). The grafting of polyphenols onto protein structures is an effective and promising way to synthesize novel functional foods with desirable physicochemical properties and antioxidative features (Shahbazi, Jäger, Ettelaie, et al., 2021). There are several studies in the literature indicating that the grafting of polyphenols onto proteins can not only enhance the functionality of the protein but also suggests the biological stability of the polyphenols (Shahbazi, Jäger, Ettelaie, et al., 2021). Recently, numerous synthetic approaches involving application of a free-radical grafting procedure were introduced to attain a stable macromolecular system, containing grafted protein-g-polyphenols (Shahbazi et al., 2022b; Shahbazi, Jäger, Ettelaie, Mohammadi, & Kashi, 2023). Based on the reaction features of free-radical grafting copolymerization, it has been proposed that the free radicals generated by alkali treatment, redox pair system, and enzymatic methods have a prevailing effect on the reaction modification of polyphenol-grafted proteins. Taking advantage of the utilization of eco-friendly reacting agents, sustainability, and cost-efficiency, the free-radical grafting by a redox pair system (such as a mixture of hydrogen peroxide and ascorbic acid) admits the effective grafting of polyphenols onto the biomaterial backbone with greater emulsion stability, slower polyphenols degradation rate, and enhanced functionality of antioxidant components (Shahbazi, Jäger, Ettelaie, et al., 2021). Presumably, hydrogen peroxide is considered to react with ascorbic acid via a redox reaction to develop ascorbic acid radical, which abstracts hydrogen atoms of reactive groups (including amino and sulfhydryl groups) on soy to develop S- and N-centered protein backbone radicals. This results in the stretching of the soy macromolecules with a reduction of intermolecular hydrogen linkages. The produced radicals of protein macromolecule, crosslink with polyphenols at the cysteine, proline, histidine, and methionine positions, develop the desired grafted protein-*g*-polyphenol.

Above all, the initial hypothesis was based on the fact that the surface modification of soy proteins with different types of polyphenols might produce a Pickering emulsion gel with improved flow behavior and printability to fabricate a 3D-printed plant-based cheese with good printing quality and well-defined geometries. To the best of our knowledge, there are no reports on producing surface-active soy with free-radical grafting as a printable ink for engineering a well-defined 3D structure.

On this basis, three different polyphenols (rosemary, thyme polyphenols, and basil polyphenols) were introduced into soy protein particles through a free-radical grafting method to develop shear-thinning, viscoelastic, and thixotropic Pickering emulsion gels for 3D printing purposes. Besides, evaluating the printing accuracy merely from the rheological and structural features of 3D printed structures was insufficient and occasionally imprecise. Thus, emulsion stability, rheological, and printability were consolidated to perform the difference of 3D objects from gel structure to evaluate the true printing performance upon rapid prototyping, which would offer valuable insight into the upcoming investigations on improving the printing performances of advanced materials during the 3D printing process.

2. Methods and materials

2.1. Materials

Soy protein isolate (SPI) (moisture content:12.1%, fat: 0.8%, protein: 93%, ash: 3.40%, pH: 7.09, and viscosity of 1% wt. Solution: 10.0 cP) was purchased from Archer Daniels Midland Company (ADM, Decatur, IL. Rosemary (total phenolic content: 144.1 ± 1.3 mg; main phenolic acid: carvacrol), thyme polyphenols (total phenolic content: 113.6 ± 0.55 mg; main phenolic acid: p-Cymene), and basil polyphenols (total phenolic content: 98.4 ± 1.2 mg; main phenolic acid: isopropyl myristate) were obtained from (Niko Shimi Co., Tehran, Iran) (Supplementary Materials, S-1 section). Folin-Ciocalteau's phenol reagent and 2,2-diphenyl-1-picrylhydrazyl (DPPH) were supplied from (Irvine, CA). L-Ascorbic acid and hydrogen peroxide (H_2O_2) were purchased from Sigma (Sigma-Aldrich GmbH, Sternheim, Germany). All other reagents used were analytical grade without further purification.

2.2. Development of SPI–g–polyphenol variants

The SPI was surface modified by rosemary polyphenols (RP), thyme polyphenols (TP), and basil polyphenols (BP) to produce grafted SPI-*g*-RP, SPI-*g*-TP, and SPI-*g*-BP based on the previously conducted work by Shahbazi et al. (2021b). In this regard, SPI (20 g) was dispersed in 100 mL of distilled water (20 wt %) and stirred through a homogenizer device at the ambient temperature for 120 min to produce a homogeneous dispersion. Next, 5 mL of redox initiator compounds (H_2O_2 (1.0 M) comprising 0.1 g of ascorbic acid) was incorporated into SPI-based dispersion. Following that, the SPI dispersion was mixed with redox initiator compounds and homogenized using an ultrasonic cleaning device at 30 kHz for 5 min. Finally, three levels (0.5, 1.5, and 3 w/w%) of polyphenols were individually added to SPI and vigorously stirred via the homogenizer device at ambient temperature for 120 min to ensure complete hydration. Blank SPI, as a control, was obtained in similar circumstances albeit without the polyphenol grafting process.

2.3. Characterization of SPI–g–polyphenols

2.3.1. Solid-state nuclear magnetic resonance

For molecular characterization, a Bruker spectrometer (Bruker AVANCE III 600, Ettlingen, Germany was employed to monitor solid-state ^{13}C nuclear magnetic resonance (NMR) spectra. In this case, a cross-polarization magic angle spinning (CP/MAS) technique with a ^{13}C frequency of 100.6 kHz. The specimens were packed into 4 mm zirconia rotors and closed with Kel-F end-caps. The samples were spun in a triple resonance probe at the magic angle with a spinning speed of 14 kHz. A ramped ^{1}H- pulse was applied during the contact time of 1 ms. To obtain satisfactory signal-to-noise proportions of the spectra, a pulse delay time of 2 s between 15 and 81 $\times$ 10^3 scans was collected (Sabet et al., 2021).

2.3.2. Fourier-transform infrared spectroscopy (FTIR)

The samples were blended with dried pure KBr powder at a ratio of 1:100. The mixtures were ground and pressed into sheets. A Fourier transform spectrophotometer (Jasco FT/IR6200, Tokyo, Japan) was then used to detect spectrum ranging from 4000 to 400 cm^{-1} with a resolution of 4 cm^{-1} for 64 scans (Santos, de Carvalho, & Garcia-Rojas, 2021).

2.3.3. Determination of grafting degree

The freeze-dried soy–polyphenol conjugate variants (5 mg mL^{-1}) were dispersed in distilled water and stirred at 30 °C for 60 min. Next, 0.5 mL of suspension was blended with 1 mL of Folin–Ciocalteu reagent (5 times dilution) and was continuously stirred for 60 min in the dark. The reaction was initiated by introducing 5 mL sodium carbonate (10 w/v%). The suspension was treated by a high-speed rotor-stator device (Ultra-Turrax, IKA* T25 digital, Germany) for 2 min, which induced a shear force at a shear rate of 400 s^{-1} (20664 G-force). The reaction was accomplished within 18 h in ambient temperature and under atmospheric pressure. Finally, the absorbance of the homogeneous dispersion was measured at 650 nm through a UV–vis spectrophotometer (UV-2550, Shimadzu, Japan). Gallic acid was used as a standard and the grafting degrees of the grafted microconjugate variants were expressed as milligrams of each polyphenol equivalent per gram of the grafted soy–polyphenol conjugates.

2.3.4. X-ray diffraction (XRD)

A Bunker D8 Advance XRD apparatus (Bruker AXS Inc., Germany) was used to determine crystalline features of SPI–g–polyphenols at 40 kV and 30 mA Cu-Kα (λ = 1.5405 Å) radiations. The XRD measurements were used with a scanning speed of 2° min^{-1} ranging from 4 to 60° (two theta). The XRD diffractograms were acquired through MDI-Jade software (V6.0) and the relative crystallinity (%) was measured using the total area and the area under diffractogram peaks (Ma et al., 2021; Shahbazi, Jäger, Chen, & Ettelaie, 2021).

2.3.5. Contact angle

The contact angle (CA) was obtained by an OCA 20 contact angle meter (Dataphysics Instruments GmbH, Filderstadt, Germany) using the sessile drop approach in natural light. A uniform thin film was fabricated using a KW-4A spin-coater (CHEMAT Technology Northridge, CA). This was achieved by spin coating of 2.0 wt % pristine and modified soy suspensions (in toluene) onto silicon wafers at a shear rate of 210 s^{-1} (5690 G-force) for 1 min. This was then followed by heat treatment at 90 °C overnight. The resulting films were sectioned 4 $\times$ 6 cm^2 and placed on a horizontal movable stage. A drop (5 μL) of deionized water with a syringe (10 μL, Hamilton, Switzerland) was deposited centrally on the surface of the films. The data were analyzed by the software offered by Dataphysics Instruments (Shahbazi et al., 2022a,b).

2.3.6. Scavenging activity on DPPH free-radicals

The DPPH free-radical test has been extensively applied to evaluate the preliminary radical scavenging capacity of plant extracts or anti-oxidant compounds. In this regard, the antioxidant evaluation was conducted by DPPH radical scavenging experiment. The DPPH solution was obtained by introducing 5.0 mg of DPPH in methanol (100 mL). The aqueous suspensions/solutions of pristine soy and grafted micro-conjugate variants were individually prepared by dispersing 50.0 mg of each sample in 100 mL of deionized water and stirring for 60 min. After introducing 5 mL of the DPPH solution to each tube, the resulting mixtures were shaken vigorously and incubated at ambient temperature in the dark for 60 min. Next, the reactants were centrifuged (Eppendorf centrifuge 5417R, Hamburg, Germany) at 4000 G-force for 5 min. Afterward, the absorbance was measured at 517 nm using a UV–vis spectrophotometer (UV-2550, Shimadzu, Japan). The ascorbic acid was utilized as the positive control. The scavenging effect of DPPH radical was measured as follows:

$$\text{Scavenging effect}\ (\%) = \left[1 - A_{s\_517nm} - A_{b\_517nm}/A_{0\_517nm}\right] \times 100 \quad (1)$$

where A_{0_517nm} is the absorbance of the control (using deionized water instead of the sample), A_{s_517nm} is the absorbance of the samples mixed with reaction solution, and A_{b_517nm} is the absorbance of the sample under the same condition as A_{s_517nm}, but ethanol was used instead of ethanol solution of DPPH (Kedare & Singh, 2011; Mishra, Ojha, & Chaudhury, 2012).

2.3.7. X-ray photoelectron spectroscopy (XPS)

The XPS assay was also conducted to further verify the grafting modification of soy. The experiments were conducted through a Kratos Axis spectrometer (Ultra Kratos Analytical, Manchester, U.K.) *via* a monochromatic Al Kα source and a 180° hemispherical electron energy analyzer, working at a pass energy of 65 eV. The step size was 0.1 eV with a dwell time of 1000 ms. The analyzed zone was adjusted at a region of 300 $\times$ 700 μm^2. A Shirley baseline was employed aimed at the subtraction of the background, and Gaussian/Lorentzian (70/30) peaks were applied for spectral decomposition. Each spectrum was analyzed through Vision software supplied by Kratos (Vision 2.2.2, Ultra Kratos Analytical, Manchester, U.K.).

2.4. Preparation of SPI–g–polyphenol emulsions

The pure SPI, SPI-*g*-RP, SPI-*g*-TP, and SPI-*g*-BP (20.0 g) were dispersed in deionized water (100 mL) and stirred at 40 °C for 120 min through a magnetic heater stirrer. An O/W emulsion was prepared by blending canola oil 10 and 90 wt% aqueous SPI-based dispersions using a high-speed blender (Ultra-Turrax T25D IKA, Germany) for 5 min followed by a sonication treatment at 30 kHz for another 5 min. The full-fat stabilized emulsion was regarded as control hereafter (10 wt % canola oil, 20 wt % SPI, pH 6.6). Separately, three kinds of SPI-polyphenol emulsion gel were prepared by the addition of canola oil (10% w/w) with the stock suspensions of SPI-*g*-RP, SPI-*g*-TP, and SPI-*g*-BP (90% w/w). In all formulations, the level of SPI was considered constant (20 wt %). All Pickering emulsion gels were conditioned in a controlled bio-chamber (ACS Sunrise 700 V, Alava Ingenieros, Madrid, Spain) at 25 °C with a relative humidity of (37 $\pm$ 1)% for 48 h.

2.5. Characterization of emulsions

2.5.1. Measurement of interfacial surface pressure

An automated drop tensiometer (Tracker-H, Teclis, France) was employed to detect the adsorption kinetics and interfacial surface pressure (π) of SPI-based emulsion or SPI–*g*–polyphenol emulsions at the O/W interface at an ambient temperature. In this regard, the oil phase and bulk phase were located at the syringe and cuvette, respectively. Before the experiment, oil and dispersions were allowed to equilibrate for 60 min to attain 25 °C. The system temperature was kept constant using circulating water from a thermostat. The O/W interfacial pressure

(π, mN m^{-1}) was calculated as follows:

$$\pi = \gamma_0 - \gamma \quad (2)$$

where $\gamma 0$ and γ (mN/m) are the interfacial tension of water and that of SPI-based emulsion or SPI–*g*–polyphenol emulsions.

2.5.2. Measurement of interfacial viscoelasticity

A sinusoidal interfacial compression and expansion method was applied to investigate the dynamic interface viscoelasticity of SPI–*g*–polyphenols at the O/W interface. Especially, the oil phase and bulk phase were located at the syringe and cuvette, respectively. With the alteration of drop volume at 10% of deformation amplitude inside the linear regime, the sinusoidal interfacial expansion and compression were investigated. During the experiments, the numbers of blank and active were 10 cycles with an oscillation frequency of 0.1 Hz. The other settings factor and trial methods were equal to section 2.5.2.

2.5.3. Rheological tests

A dynamic shear rheometer (Kinexus, Malvern, Worcestershire, UK) was utilized to investigate the frequency sweep with cross-experiments over the emulsions. The frequency sweep experiments were performed as a function of shear rate (0.1–101 Hz) within the linear viscoelastic region (a fixed strain at 1%), in which changes of storage modulus (G') and loss modulus (G'') were obtained.

In addition, to gather data on the thixotropy of the emulsion-based ink, a five-interval thixotropy test (5-ITT) was applied at ambient conditions, detecting the viscosity profiles of the inks under alternating high and low shear rates (90 or 0.1 s^{-1}) for 140 s and 160 s, respectively.

2.6. Printing process

Prusa i3 is named after the third repetition of the design by Josef Průša. All parts of this 3D printing system were open-source and were part of the 3D Food Printer project. Table 1 resumes the main characteristics and Fig. 1 depicts the original Prusa i3 Printer assembly kit and an assembled printer.

The component of the syringe unit was designed through SolidWorks™ (Dassault Systèmes, SolidWorks Co., Vélizy-Villacoublay, France) and was developed by Peyman Asghartabar Kashi and was 3D printed from polylactic acid (PLA, eSUN, China) using a homemade extrusion-based 3D printer. We decided to fabricate the components of the syringe unit with another 3D printer than the device we aimed to modify, as this facilitated design optimization and circumvented the need for multiple assembly-disassembly-cycles, accelerating the prototyping procedure.

The machine architecture is very simple, where the extrusion head transfers in the XZ plane construction while the platform translates along the Y-axis (Fig. 1). The horizontal translation of the head is controlled by the X-axis and the vertical translation allows the increment along the Z-axis. The mechanical structure is minimal and contains fundamentally two rails along which the building platform is moved, the other two rails for the motion of the extrusion head, and the structure to support the rails.

Table 1
Technical specifications of Prusa i3.

Technical specifications	Empty Cell
Build volume (mm^3)	200 × 200 × 180
Supported materials	ABS, PLA
Number of extruders	1
Heated platform	Yes
Minimum layer thickness (mm)	0.1
Syringe diameter (mm)	30
Nozzle diameter (mm)	2
Open Source	Hardware and software

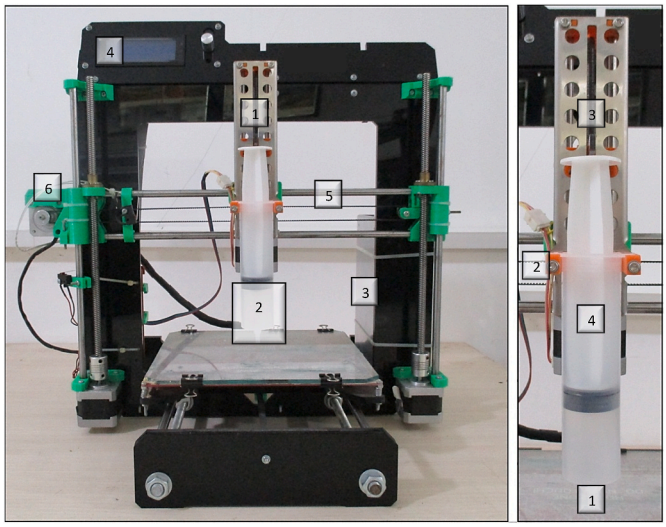

Fig. 1. Schematic of the retrofitted Prusa i3 printer (**A**) including (1) syringe driver, (2) 60 mL syringe, (3) power supply unit, (4) controller unit for the printer, (5) support rods for the printer, (6) support rods and motor for the printer. (**B**) Schematic of the printer extruder including (1) the nozzle, (2) 3D printed parts, (3) laser cut parts (4) 60 mL syringe. The printer was connected to and controlled by an Arduino mega 2560 with a marlin framework and Cura slicer.

For the 3D printing process, a square (40 mm, 40 mm, 10 mm height) was initially modeled and converted into.STL files through the computer-aided design software (SolidWorks™, Dassault Systèmes, SolidWorks Co., Vélizy-Villacoublay, France). Next, the Cura™ slicing software (V. 2.3.1., Ultimaker, Geldermalsen, Netherlands) was used to convert.STL files to G-Code files. A nozzle with an inner diameter of 2 mm was employed to extrude Pickering emulsion gels on a silicon platform using a direct-ink-write (DIW) 3D printing process. After comprehensive consideration, emulsions with improved flow behavior were designated for printing process, with layer height being 1.2 mm, shell 2 mm, and nozzle movement speeds during printing being 20 mm s^{-1} (Shahbazi et al., 2022b). The main printing process was carried out at temperature ambient temperature.

2.7. Oral tribology measurements

Saliva has an important effect on oral lubrication and must be introduced in a tribological experiment aimed at a desired simulate of the in vivo circumstances. The unstimulated whole saliva (4 mL) was collected according to established work by Shahbazi et al. (2022b) with some modifications. In short, ten non-smoker participants (five females and five males) were trained to refrain from eating or drinking (excluding water) for 2 h before the saliva collection in the morning (10 a.m.). Next, the participants were requested to rinse their mouth with water four times, and then saliva was collected by chewing a silicone cube (35 mm diameter). The participants put the cube in their mouth with water (5 mL) and started to chew for 40 s and then expectorated. In the end, they were asked to continue chewing for 50 s, simultaneously collecting saliva in a 100 mL sterile container served on ice. Approximately 4 mM imidazole/acetate buffer (pH 7.0) was added to the freshly collected saliva (1:1 v/v) and centrifuged (Beckman, GS-15R Palo Alto, CA) at 2000 G-force for 5 min. The imidazole/acetate buffer (pH 7.0) was further incorporated into the supernatant to dilute it to 16 (v/v)% of the unstimulated whole human saliva for tribological analyses and stored at −18 °C for further test.

To evaluate the lubricant properties of the 3D printed objects, oral tribology evolution of saliva (*ex vivo*) was performed using a ring-on-plate tribo-rheometry (TA Instrument, New Castle, DE) on a rough

hydrophobic surface of 3M Transpore Surgical Tape 1527–2 (3M Health Care, St Paul, Min), which was the state to have a comparable surface roughness ($R_a = 31.5$ μm) and wettability to the human tongue. A half-ring rheometry was utilized to provide the refill of material between the two solid surfaces. The tape was cut in a square form and compacted tightly on top of the lower plate rheometry. After each measurement, the tape was relaced and the instrument was cleaned with deionized water. The extent of 3D printed samples was sufficient to cover the surface of the substrate and offered a thin film. To mimic the sensory investigation process, the normal forces of 2 N were used to denote the adequate normal force employed upon oral processing. Moreover, the oral condition was mimicked at a temperature of 37 °C. Each 3D printed object was pre-sheared at a speed of 0.02 s^{-1} for 2 min, and after that equilibrated for 1 min before each measurement. The human tongue was reported to move at a speed of 200 mm s^{-1}. Therefore, the tribology assay in the current study was within this range. Afterward, the increasing rotational speed ramp was set from 0.01 to 200 mm s^{-1} with the attainment of 25 points per decade. The values of the coefficient of friction (*CoF*) were determined as the friction stress (σ_F) proportion to the normal stress (σ_N), described by Eq. (3):

$$\mathrm{CoF} = \sigma_F/\sigma_N = M/F_N \times (r_2 + r_1)/\left(r_2^2 + r_1^2\right) \quad (3)$$

where M is torque (Nm) and F_N is normal force (N), r_1 is the ring inner (14.5 mm) and r_2 is the outer radius (16 mm).

Moreover, the coefficient of friction was plotted versus the increasing sliding speed as follows:

$$\nu_s = \overline{\mathrm{R}} \times \omega \quad (4)$$

Here, ν_s is the sliding speed (mm s^{-1}), $\overline{R}$ is the mean of the ring's inner and outer radius, and ω is the controlled rotational speed (rad s^{-1}).

2.8. Temporal dominance of sensations (TDS)

2.8.1. Selection of terms and panel instruction and training

Ten assessors (five females and five males, aged: 24–34 years) participated in this study. They were designated based on the guidelines of the ISO 8586:2012 standard and familiar with the sensation of cheese analogue products. Two 1-h preliminary sessions were conducted to define the TDS methodology and the notion of the temporality of sensations, offering the participants the chance to investigate the data collection software and get acquainted with it. The repeatedly stated sensory features were selected and their descriptions to assess them were defined. The nine selected attributes for 3D printed cheese analogues objects were listed as firmness, thickness, creaminess, graininess, mouth-coating, smoothness, chewiness, fattiness aftertaste, and residue aftertaste. Each attribute reference, applied to acquaint the panelists, is shown in Table A-1 in Supplementary Materials. The assessors were afterward trained to employ the computerized TDS data capture system (FIZZ v 2.40A) according to the procedure defined by Pineau et al. (2009). The assessors needed to place the 3D-printed samples into their mouths and click on the start button to begin the assessment. At 15 s, they were asked to swallow the printed objects via a message presented on the screen and continue the assessment until no attributes were perceived. Then, panelists were trained to click the stop button excluding data acquisition had automatically stopped upon the time of 60 s. The evaluators were afterward requested to recognize the sensory attributes they perceived as dominant while conducting the testing procedure. The evaluators were also informed that they did not have to choose all the attributes in the list and that they could select a similar sensation multiple times during the assessment or in contrast never choose a descriptor as dominant.

2.8.2. Formal assessment

The dynamic sensory properties through TDS method was employed to express variances in the dynamic sensory profile of 3D-printed cheese analogue variants. The TDS evaluation was performed over three sessions to run three replications. The 3D printed objects (3 × 3) cm^2 were provided to the assessors by the randomized complete block design in a monadic order. The panelists were then offered a list of nine sensations on the computer screen, each related to an unstructured scale anchored from weak to strong. The normalized time was plotted against the dominance rate of each trait at a given point in time (%). Each curve displayed the progress of the dominance rate of an attribute over time. In this sense, FIZZ software (Version 1.9, Biosystems, Counternon, France) was utilized to obtain the TDS plots. To better illustrate, smoothed TDS curves were plotted through MATLAB software (R2016a, MathWorks Inc., Natick, Ma). Two lines were displayed on each TDS graph, namely chance- and significance levels to simplify the interpretation of attributes. The chance level signifies the minimum magnitude of a dominance rate that a trait was attained by chance (1× (number of attributes)$^{-1}$). The significance level states the least magnitude of a dominance rate of a given trait, which is significantly higher than the chance level ($P < 0.05$).

2.9. Statistical analysis

Unless otherwise stated, all measurements were carried out in triplicate. One-way analysis of variance (ANOVA) with a 95% confidence interval was used to compare the significance of the results obtained. Statistical analysis was performed using SPSS software version 19.0.

3. Results and discussion

3.1. Characterization of SPI-g-polyphenol conjugates

3.1.1. Analysis of reactive group contents

Free-radical associated grafting was used to develop SPI–polyphenol conjugates, where a blend of hydrogen peroxide and ascorbic acid, as a redox initiator compound, develops hydroxyl radicals (·OH) using anoxidation–reduction reaction (Geng et al., 2022). This method with low toxicity is cost-effective and sustainable and is frequently served in the grafting of polyphenols with numerous macromolecules such as chitosan (Jing, Diao, & Yu, 2019; Mittal, Singh, Aluko, & Benjakul, 2021), whey (Nair et al., 2020), soy (Zhou et al., 2020), gluten hydrolysate (He et al., 2022), and egg white protein (Gu et al., 2022). Practically, free-radical grafting can be achievable at ambient temperature, therefore lowering the degradation or deterioration of polyphenols or proteins.

Fig. 2a shows the possible mechanism of free-radical-induced grafting methods. An ascorbate ion is developed as a result of the oxidation of ascorbic acid, which additionally gives pair of electron or hydrogen ions in the presence of hydrogen peroxide. Next, resonance-stabilized tricarbonyl ascorbate free radicals are produced using ascorbate radicals. Following that, the previously developed electrons or hydrogen ions react with hydrogen peroxide to create ·OH. Subsequently, hydrogen is abstracted from amine and/or hydroxyl groups of SPI through hydroxyl radicals, generating protein-macroradicals. Ultimately, polyphenols existing in the system can be attached to SPI macroradicals. polyphenols are recognized to be excellent hydrogen donors, which can generate hydrogen linkages with the C═O group of protein molecules (Curcio et al., 2009; Liu, Sun, Yang, Yuan, & Gao, 2015).

The hydrogen atoms located at hydroxyl, amino, or sulfhydryl sites on the protein were excited by hydroxyl radicals attack, developing intermediate radical species that finally reacted with polyphenol variants to produce grafted conjugates (Curcio et al., 2009). The amount and position of hydroxyl groups (Liu et al., 2015) and the number of the aromatic rings (Shahbazi et al., 2021b) considerably affected the activity of covalent reactions and the grafting degree of proteins and polyphenols. As shown in Fig. S-1 (Supplementary Materials), most phenolic compounds of RP, TP, and BP contain carvacrol, p-Cymene,

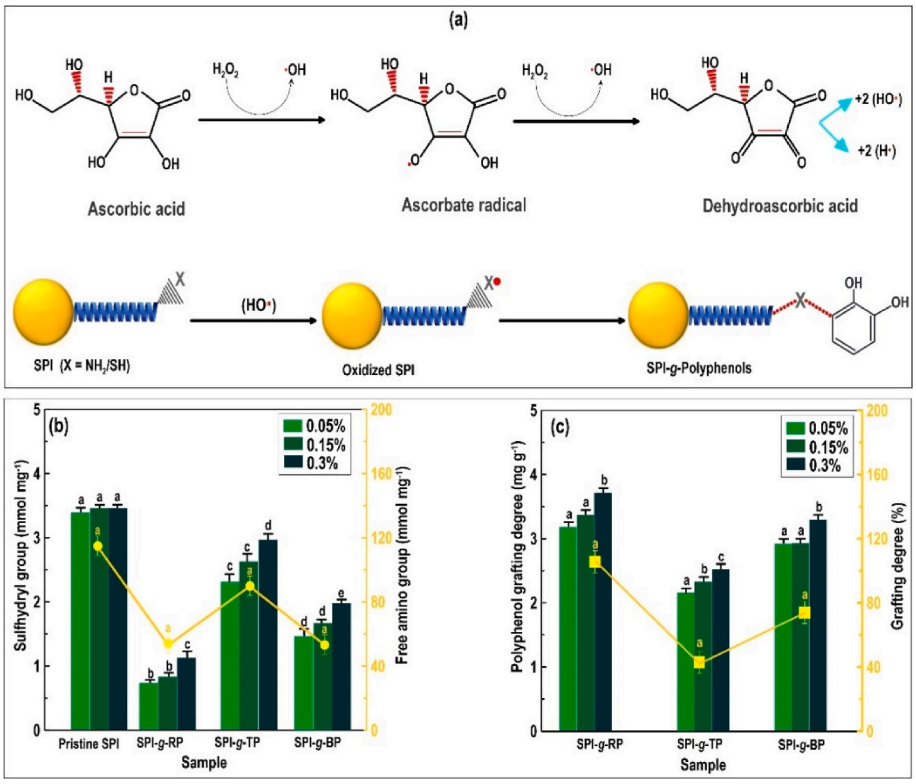

Fig. 2. (a): The mechanisms of free radical-induced to prepare SPI–polyphenol conjugates, (b): Contents of free amino and sulfhydryl groups of SPI and SPI–polyphenol conjugates (c): amounts of polyphenols bound within SPI–polyphenol conjugates.

and isopropyl myristate, respectively. Moreover, the protein radicals typically attack hydroxyl groups of polyphenols at the ortho- or para-positions (Cao & Xiong, 2015). Hence, differences in the grafting degree of SPI–polyphenol conjugates could be associated with individual variations in phenolic hydroxyl content, total phenolic content, and free radical binding sites.

To assess a possible grafting reaction between the phenolic compounds and proteins, the highly reactive nucleophilic groups of free sulfhydryl groups and amino in soy proteins can be considered (Zhou et al., 2020). Fig. 2b shows the variations in the sulfhydryl and amino extents of the neat (unmodified) SPI and grafted SPI–phenolic compounds obtained through the three types of polyphenol extracts. Concerning SPI-*g*-RP and SPI-*g*-BP, the contents of the sulfhydryl and amino groups in the protein were notably decreased, possibly because of the development of hydroxyl radicals as affected by hydrogen peroxide and ascorbic acid with the NH_2 or SH groups on the protein backbone. The produced protein radicals then attack the adjacent functional groups of phenolic components, producing protein-*g*-phenolic conjugates through C–S and C–N linkages. Similar results were reported in a previous publication by Liu, Xu, Zong, Yu, and Zhang (2021), who developed the protein conjugates with the application of four different dietary polyphenols using free-radical grafting. They also assumed that a decrease of the amount of free amino amounts and sulfhydryl groups in the protein and simultaneously increase in the molecular weight of grafted complex, established the development of covalent linkages between the protein and the polyphenol variants. In the current work, the sulfhydryl extent of SPI-*g*-TP was only slightly decreased relative to that of the neat SPI, though, the number of amino groups was considerably reduced because of the activation of the carboxyl groups of TP by the redox initiator compound to produce an amide bond with the protein amino group (Ye, Fan, Xu, & Liang., 2013). Similar results were stated by Yan, Xu, Zhang, and Li (2021) who detected a new amide bond developed by an amide reaction among the carboxyl group of gallic acid and an amino group in SPI.

To develop the optimum of SPI-*g*-polyphenol conjugates, the grafted conjugate variants including a different type of polyphenols (RB, BP, and TP) to SPI (00.5, 1.5, and 3% w/w) were obtained. Next, the degree of grafting was measured by evaluating the polyphenol amounts. From Fig. 2b, with an increasing mass ratio of up to 3% the grafting degree increased significantly ($P < 0.05$). Thus, the SPI-*g*-TP, SPI-*g*-BP, and SPI-*g*-RP samples with a mass ratio of polyphenols to SPI of 3% (w/w) were selected as the optimum grafted conjugates for the following instrumental characterization.

3.1.2. FT-IR analysis

The addition of new steric, functional phenolic components to the protein backbone changes the structure properties and physicochemical features of the protein. Fig. 3a shows the FT-IR spectra of neat SPI and grafted SPI-polyphenol conjugates. Regarding neat SPI, a long, broad characteristic band located at 3352 cm^{-1} occurred because of the tensile vibration of intermolecular hydrogen linkages of hydroxyl and amino groups. This is also referred to as amide A, which assigns to the N–H stretching coupled with hydrogen linkages (Yan et al., 2021). After the synthesis of grafted SPI–polyphenols, this peak position moved from 3352 cm^{-1} to around 3250 cm^{-1}, showing that the interaction between SPI and polyphenols was induced by hydrogen linkages. Simultaneously, the magnitude of hydrogen bonds was also affected by the type of polyphenols, in which RP decreased the area of O–H and N–H groups (Fig. 3a). This could be due to the involvement of more phenolic groups (Fig. S-1, Supplementary Materials) in the system, promoting the development of strong hydrogen linkages among SPI and RP. Concerning neat SPI, an absorption peak at 2880 cm^{-1} could be associated with the C–H tensile vibration of methyl and methylene groups of SPI (amide B). The alterations of thus described peak position were also evaluated to explore whether hydrophobic interactions occurred amongst protein and polyphenol variants. The peak position of all SPI-polyphenol conjugates showed a shift from 2880 cm^{-1}–2913 cm^{-1} in comparison with neat SPI. This specifies that hydrophobic interactions occurring between

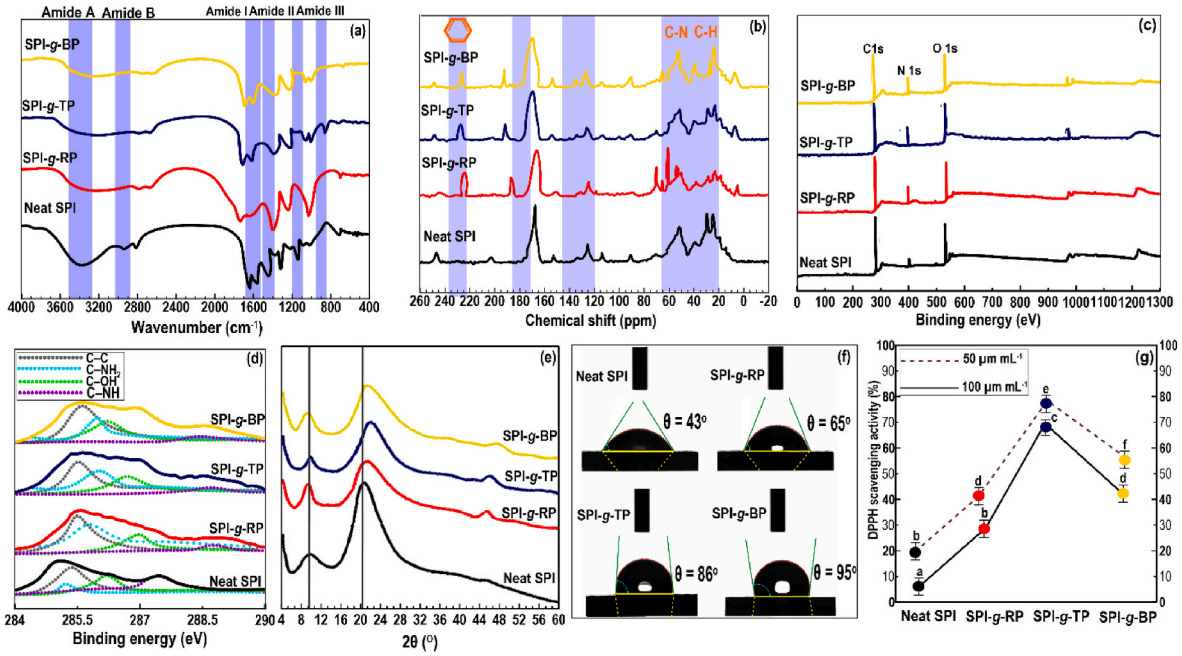

Fig. 3. Characterization of grafted soy–polyphenol conjugates. (a): FTIR; (b): solid-state ^{13}C NMR; (c): XPS; (d): XPS resolved peaks; (e): XRD; (f): water contact angle; (g): DPPH free-radical measurement. In the case of antioxidant features, the means inside each column with various letters (a–f) are significantly different ($P < 0.05$) according to Duncan's test.

protein and polyphenols upon the development of the grated conjugates (Ye, Fan, Xu, & Liang, 2013). Furthermore, the hydrophobic interaction was principally not affected by polyphenol types. This could be a result of the high level of phenolic content, which induces protein aggregation and hinders the hydrophobic interactions among polyphenols and interior hydrophobic groups of SPI (Dai et al., 2022).

The grafting reaction of SPI and polyphenols is also expected to lead to a considerable loss of four typical peaks associated with NH_2 (amide I, II, and III), whereas emerging new bands belong to the development of graft conjugation (Yan et al., 2021; Ye et al., 2013). The spectrum of neat SPI displayed typical bands associating with amide I around 1662 cm^{-1} (assigned to C═O stretching), amide II at 1462 cm^{-1} (related to N–H bending), and amide III around 1167 cm^{-1} (N–H deformation and C–N stretching) (Yan et al., 2021). The grafting of phenolic components onto the SPI led to an obvious change in the FT-IR spectral intensity and peak positions of these regions. After introducing different types of polyphenols, the peak of amide I from around 1662 cm^{-1} moved to 1701 cm^{-1}, while the amide II band from 1462 cm^{-1} decreased to 1328 cm^{-1}. Further, the absorption bands of amide III were found to interestingly disappeared in comparison with neat SPI, signifying that N–H and C–N groups actively interacted with polyphenols with losing a certain number of amino groups. The emergence of the typical band around 1100 cm^{-1} also proposed that a notable amount of hydrogen linkages was possibly demolished during grafting (Shahbazi et al., 2022b).

Compared to SPI-*g*-TP and SPI-*g*-BP, the peak intensities of the amide I of the SPI-*g*-RP were broader and stronger, representing that the polyphenols are effectively grafted onto the SPI, developing more amide bonds. These results are following the changes in the sulfhydryl and amino extents of the grafted SPI–phenolic compounds (Fig. 3a). Moreover, in the spectrum of SPI-*g*-RP, the intensity of the amide II band was appreciably increased relative to those of SPI-*g*-TP and SPI-*g*-BP, representing that more C–N stretching modes combined with N–H bending vibrations contribute to more absorption of the amide II band. Furthermore, the increased peak intensities are attributed to the increase in the number of amide linkages arising from the binding of phenolic compounds to the proteins (Sui et al., 2018). In addition, a new band around 950 cm^{-1} appeared on the FT-IR spectrum of the SPI-*g*-TP complex, which is associated with the C–O stretching vibration of the phenolic OH group, further verifying the TP was efficiently grafted onto the SPI (Li et al., 2022).

3.1.3. *Solid-state ^{13}C NMR spectroscopy*

To investigate the chemical structure and interactions between the added polyphenols and SPI, the solid-state ^{13}C cross-polarization/magic angle spinning nuclear magnetic resonance method was performed. The solid-state ^{13}C NMR spectra of neat SPI and grafted SPI-polyphenol conjugates are presented in Fig. 3b. The NMR spectrum of SPI comprises the typical peaks of soy protein, including methyl and methylene groups (16–24 ppm), β-carbons (26–44 ppm), α-carbons (46–67 ppm), aromatic rings (116–132 ppm), carbonyl groups (167–182 ppm) (Chen, Zhang, et al., 2021). Compared to polyphenols-coated SPI, the change in the NMR spectrum of grafted SPI-polyphenols was more noticeable with the emergence of several new peaks at 6 ppm and 38 ppm. While, the band at 16–24 ppm, assigned to the methylene groups, became more intense. This possibly results from the presence of terminal methyl carbons, *i.e.*, the secondary carbon ($-CH_2-$) and the primary carbon groups ($-CH_3$), which are in agreement with the FT-IR spectrum. Meanwhile, a comparatively broad peak occurred around 190 ppm, which relates to the resonance of the carbonyl ester (C═O). This result also was following the carbonyl stretching vibration around 1869 cm^{-1} detected by FT-IR assay. Therefore, the polyphenols through free radicals were supposed to develop chemical reactions with SPI chains. Furthermore, the NMR spectrum of SPI-*g*-TP was almost the same as that of SPI-*g*-BP, except for additional NMR peaks at 240 ppm, which were caused by C–N the soy protein.

3.1.4. *XPS measurement*

XPS analysis is a powerful device to monitor the changes in the chemical component's distribution of the SPI as affected by surface modification since the outermost 6 nm depth of the surface layer (45 Å) was measured. Fig. 3c shows that the surface of the SPI mostly included carbon (C 1s), nitrogen (N 1s), and oxygen (O 1s). After surface modification of SPI, the XPS pattern of SPI-polyphenol conjugates was similar to the neat SPI with no emergence of obvious new bands. In these cases,

however, the intensity of the typical peaks around 400 eV was remarkably increased, which were related to the aromatic C=N and aromatic C–N. This further proposed the successful grafting of polyphenols onto the SPI backbone.

The peak area of C 1s, O 1s, and N 1s, as well as the O/C and N/C ratios, can reflect the level of carbon, oxygen, and nitrogen atoms on the surface. The C 1s specifies the hydrophobic character of the surface and O 1s, and N 1s reveal the content of hydrogen interaction in SPI materials. With the comparison of the percentage level of these atoms, the level of carbon increased after polyphenol grafting, whereas the level of oxygen decreased. That is to say that, the surface hydrophobicity of SPI materials was increased after developing grafted SPI-polyphenols conjugates.

Fig. 3d shows an analysis of the scanning spectrum of element C 1s. The spectrum plot of this element for each individual sample is further deconvoluted to explain the change in the C status in the sample, including C1(C–C), C2(C–NH_2), C3(C–OH), and C4(–NH–CO–) (Lin, Chen, Bian, & Fan, 2012). C1 shows the hydrophobicity of compounds, and C2, C3, and C4 present the content of active functional groups in samples. The absorption bands of spectra reveal the difference in the element amount between samples. In this regard, the grafting of polyphenol components could develop strong interactions between nonpolar groups. Compared to SPI-*g*-TP and SPI-*g*-BP, the C 1s content (and therefore C1, C2, C3, and C4) of SPI-*g*-RP was higher, showing a higher hydrophobic feature, which is in agreement with the FT-IR and NMR measurements. Furthermore, the O/C proportion reduced from 0.35 to 0.30, representing that the grafting process decreased the relative level of O on the SPI surface. In contrast, the N/C proportion was increased notably, demonstrating that the level of functional amino groups of SPI-containing polyphenols increased.

3.1.5. XRD experiment

The crystalline changes between the neat SPI and grafted SPI-polyphenol conjugates were characterized by XRD assay, and the results are presented in Fig. 3e. Two characteristic peaks around 10° and 20° emerged on the diffractograms of all samples. They show α-helix and β-sheet crystal structures, assigning to the typical SPI secondary structure configuration of soy proteins. Compared to native SPI, the intensity of the α-helix peak in SPI–polyphenol conjugates spectra increased, showing an increased in the level of crystalline arrangement and increased the secondary structure of soy protein. The greatest increase of α-helix peak intensity was detected in the SPI-*g*-RP, showing a notable redistribution of the basic crystal lattice. Concerning grafted SPI-polyphenol conjugates, the typical peak of the β-sheet structure slightly moved to the higher 2θ degrees, which proposed that d_{001} spacing (gallery spacing) from d_{001} = 4.1 Å (2θ = ~20°) decreased to d_{001} = ~3.8 Å (2θ = ~21°). The shift of pronounced peaks to the higher 2θ degrees relates to a decreased in the corresponding interlayer spacing, which proposes that the materials offer a high-level of ordered structure (Guinier, 1994). Therefore, the interaction of functional groups of polyphenols with soy proteins through surface-free radical grafting leads to a change in the spatial structure and unfolding of protein molecules, increasing the chain mobility. Furthermore, the intensity of β-sheet reflection for SPI–polyphenol conjugates reduced and widened, representing that a part of the crystal structure of the protein was disrupted. This might be due to an effective interaction of polyphenols as the results of grafting reactions laeding to a lesser hydrophilic sites on the surface, which reduced the crystallinity of the soy protein adhesive. A similar fact was reported in a previous work (Shahbazi et al., 2021b; Xu et al., 2021). Interestingly, a new distinctive band around 2θ = 46° (d_{001} = 6.5 Å) emerged on the diffraction pattern of all SPI–polyphenol conjugates. This specifies the induction of a newly developed crystalline domain in the amorphous area of SPI owing to the polyphenol grafting process.

3.1.6. Contact angle

Surface hydrophobicity is related to the ability of a liquid to preserve contact with a surface of a solid, which shows the magnitude of the intermolecular interactions of a system. For this reason, the surface hydrophobicity of neat SPI and grafted SPI-polyphenol conjugates, prepared as a model thin-based film, were detected by surface contact angle meter by the sessile drop method. The results of the surface modification of SPI are presented in Fig. 3f. The contact angle of neat SPI film was detected to be 43°, showing water droplet was completely absorbed into the soy film after 60 s. Apparently, water has a much stronger interaction with the surface of neat SPI, proposing that the neat soy protein-based film intrinsically displays a hydrophilic character. Furthermore, after surface grafting of polyphenols onto SPI, the contact angle of SPI film progressively increased to 65, 86, and 95° concerning SPI-*g*-TP, SPI-*g*-BP, and SPI-*g*-RP, respectively. Once polyphenols are coated onto the SPI, the phenolic hydroxyl groups of polyphenols interacted with hydroxyl, carboxyl, and amino groups of SPI, decreasing the hydrophilic groups on the surface of the protein, consequently enhancing the surface hydrophobicity.

3.1.7. Antioxidant activity

Different in-vitro chemical-based analyzes can be employed to determine antioxidant activities such as ferric reducing capacity, DPPH radical scavenging method, oxygen radical absorbance capacity, β-carotene-linoleic acid system, etc. Depending on the reactions included, these in-vitro antioxidant experiments are commonly categorized into two types: the analyses according to electron transfer (ET), and the ones based on hydrogen atom transfer (HAT) reactions. In the current work, the DPPH assay was designated to measure the antioxidant feature of the grafted SPI-polyphenol conjugates. The grafted SPI-polyphenol conjugates displayed significantly higher ($p < 0.05$) scavenging activity on DPPH radicals compared to neat SPI (Fig. 3g). It has been reported that grafting polyphenols onto SPI offered considerably improved antioxidant features. Compared to SPI-*g*-RP and SPI-*g*-BP, the scavenging activity of SPI-*g*-TP on DPPH radicals was higher, which proposed that the antioxidant activity would be adjusted using changing the types of polyphenols (Kedare & Singh, 2011; Mishra et al., 2012).

3.2. Characterization of SPI–g–polyphenol emulsion-based inks

3.2.1. Droplet size and morphological evaluations

The manufacturing of high-quality well-defined 3D printing foods is strongly dependent on the production of a printable emulsion-based ink with a lower droplet size and monomodal particle size distribution. Based on the literature, a decrease in particle size improves the ink functionality enhancing the resolution of deposited layers and printing precision (Lee, Won, Kim, & Park, 2019; Wu et al., 2016). The particle size distribution (*PSD*) and mean droplet size ($d_{3,2}$) in the O/W emulsions, stabilized by neat (unmodified) SPI and grafted SPI-polyphenol conjugates, are presented in Fig. 4a and b, respectively (Supplementary Materials, S-2 and S-3 sections). Regarding the emulsion formulated by unmodified SPI, there is a small peak around 1 μm (Fig. 4a), which is most likely because of the presence of some SPI particles dispersed into the bulk oil phase. The *PSDs* of all SPI-*g*-polyphenol inks, by contrast, showed a more uniform in comparison with neat SPI-based emulsion, suggesting that the binding of the phenolic compounds onto soy protein particles enhance their emulsification. Furthermore, the distribution was monomodal, which proposes the lack of development of stable flocs during the *PSD* measurement (McClements, 2004). This could be due to an increase in the surface hydrophobicity (Fig. 3f) of the soy protein particles resulting from the phenolic compound grafting, which improves its surface activity at the O/W interface (McClements & Gumus, 2016). Alternatively, the grafting of phenolic compounds onto proteins can increase the thicknesses and charge density of the lipid droplets, which improves their flocculation stability using an increased steric and electrostatic repulsion among droplets (Shahbazi et al., 2021c, 2022b).

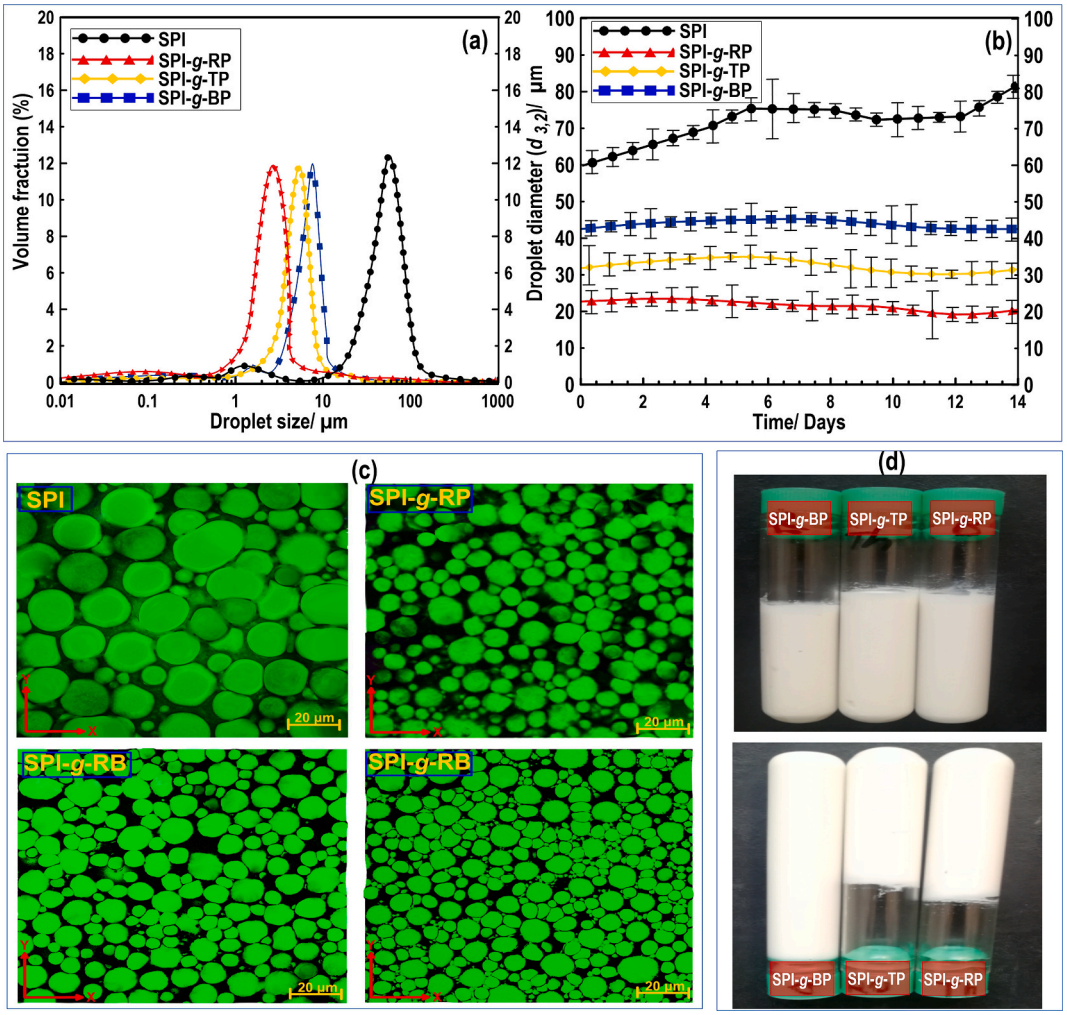

Fig. 4. (a): Droplet size, (b) particle size distribution, (c): CLSM images; (d): visual appearance of grafted SPI–*g*–polyphenol emulsion-based inks.

Fig. 4a also shows that the particle size of SPI-*g*-RP emulsion experienced a greater degree of reduction compared with those of SPI-*g*-TP, and SPI-*g*-BP inks. The better emulsifying property of grafted SPI-RP can be related to the existence of higher numbers of phenolic groups (Fig. S-1, Supplementary Materials) to interact with oil, accordingly more hydrophobic character of grafted SPI-RP (Fig. 3f). This result is also consistent with the observed molecular structure by FT-IR (Fig. 3a), NMR (Fig. 3b), and XPS (Fig. 3c), in which an increased number of nonpolar interactions resulted from a decrease in the hydrophilic groups of SPI (carboxyl, amino, sulfhydryl, and hydroxyl groups) due to interaction with phenolic functional groups of RP (Yan et al., 2022).

Fig. 4b shows that the original size ($d_{3,2}$ values) of the oil droplets stabilized by neat SPI decreased from about 60 to 43, 32, and 23 μm after preparation of SPI-*g*-TP, SPI-*g*-BP, and SPI-*g*-RP conjugates, respectively. Over time, the values $d_{(3,2)}$ of the emulsion system containing neat SPI considerably increased after 14 days (from 60 to ~83 μm). The phenomenon might be associated with the dissociation of thin surface film among the colliding droplets (coalescence) or separation of the adsorbed layers between two droplets (flocculation). The sharing flocculation phenomenon is predominant in the concentrated emulsions with the lack of biosurfactant or a low ratio of emulsifier to oil, and less concentrated systems comprising a mixture of biosurfactant with different surface activities. On the other hand, the size of the oil droplets comprising grafted SPI-polyphenol particles was stable for more than 14 days (Fig. 4b). This shows the coalescence and/or flocculation did not happen in the system. An increase in the viscosity of the continuous phase offered by polyphenol-coated SPI might be justified by the stabilizing effect of SPI-*g*-polyphenol conjugates. Additionally, the presence of intermolecular interactions between hydrophilic/hydrophobic groups in the system contributes to the biosurfactant's effectiveness on aging (Dickinson, 2003; Shahbazi et al., 2022a). Compared to SPI-*g*-TP and SPI-*g*-BP emulsions, the $d_{(3,2)}$ values of SPI-*g*-RP ink were lower (~20 μm) for more than 14 days due to a more hydrophobic feature of SPI-*g*-RP conjugate (Fig. 3f).

CLSM was utilized to characterize the microstructure of O/W emulsions stabilized by neat SPI and SPI-*g*-polyphenol conjugates (Fig. 4a). The images of the emulsion microstructure show the effective development of O/W emulsions with SPI-*g*-polyphenol conjugates. Though, there is the presence of some big oil droplets in the ink stabilized by neat SPI because of the coalescence of oil droplets. In contrast, the size of droplets obviously reduced after the preparation of emulsions stabilized by polyphenol-coated SPI, which was in accordance with the results of *PSD* and $d_{(3,2)}$ experiments. Combining *PSD* and microstructure of emulsions, it was concluded that SPI-*g*-RP inks showed better stability with lower droplet sizes compared to SPI-*g*-TP and SPI-*g*-BP inks, which could be associated with increased emulsifying features of RP induced by the higher hydrophobicity and possessed multiple surface-active sites at the O/W interface.

3.2.2. *Emulsion rheology experiments*

Appropriate printable inks for 3D printing must demonstrate a shear-thinning behavior to effortlessly flow through a nozzle tip and show a

high enough viscosity after the 3D printing process to stick to the previously deposited layers of ink (Shahbazi & Jäger, 2020). The viscosity and stress profiles of ink samples with different formulations are shown in Fig. 5a and b. As the stress-strain curves presented, all emulsions offered a shear-thinning feature, which becomes Newtonian at high shear rates (Dickinson, 2010). Compared to emulsions stabilized by neat SPI, the inks formulated by SPI-*g*-polyphenols showed much higher viscosity values. Furthermore, the ink containing SPI-*g*-RP presented the highest viscosity value, possibly because of the high level of flocculation of emulsion droplets (Dickinson, 2019). For unmodified globular protein-coated oil droplets the electrostatic repulsion between the oil droplets decreases in the pH close to the isoelectric point of the adsorbed protein, leading to droplet aggregation (Dickinson, 2010; Shahbazi, Jäger, Ettelaie, et al., 2021). The flocculated emulsions establish both improved shear-thinning features and higher viscosity compared to the non-flocculated emulsion since the aggregates preserve some of the continuous phases inside their structures, which results in improved viscosity. Upon the applied shear, the break down of the flocculation structure results in a shear-thinning property. Therefore, the inks stabilized by SPI-*g*-polyphenol conjugates displayed appreciably higher viscosity values, offering higher droplet flocculation. Once all aggregates are broken at higher shears, one expects and indeed finds Newtonian behaviour.

The viscosity measurement and flow properties have been proposed as the main functional characteristics of printable inks for the 3D printing process. The flow properties alone, though, cannot explain the complex feature of inks during printing. The oscillatory shear measurement is commonly used to concurrently assess the viscoelastic properties of printable ink. It has been stated that a viscoelastic ink can effectively uphold its geometrical shapes during 3D printing, particularly offering beneficial properties essential for the design of 3D objects with complex structures (Hardin, Ober, Valentine, & Lewis, 2015). Fig. 5c shows the elastic (G') and viscous (G'') parameters as a function of oscillatory frequency (ω) for printable inks within the linear viscoelastic region (LVR), which specifies the degree of flocculation degree of the emulsion system (Aben, Holtze, Tadros, & Schurtenberger, 2012). At the low shear rate (<1 Pa), $G'(\omega)$ of all emulsions was higher than $G''(\omega)$, which shows a characteristic gel-like structure. Concerning the emulsion stabilized by neat SPI, a quasi-solid property was found at the low frequencies (<1 Hz), in which $G'(\omega) > G''(\omega)$. However, as the frequency proceeded, a local monotonic increase in moduli was detected, where the $G''(\omega)$ progressively reached $G'(\omega)$ until a crossover point (ωc), i.e., $G'(\omega) = G''(\omega)$. This proposes a collapse or destruction of emulsion gel structures with the development of a characteristic liquid-like behavior. Alternatively, the moduli of the Pickering emulsion gel-based inks showed a fairly linear increase with increasing angular frequency, but $G'(\omega) > G''(\omega)$ throughout the frequency sweep measurement, showing a gel-like behavior. This signifies that the $G'(\omega)$ values of all SPI-*g*-polyphenols prevailed $G''(\omega)$ with no ωc point from 0.1 to 100 Hz. What's more, the magnitude of $G'(\omega)$ was remarkably enhanced regarding SPI-*g*-RP ink, showing an aggregated network. This again might have been because of the development of a structured strong emulsion owing to the higher hydrophobicity of SPI-*g*-RP conjugate (Fig. 3f).

Besides the above-mentioned rheological measurements, the appropriateness of emulsions to produce printable inks also depends on other functional features concerning the thixotropy properties. Thus, in the current study, a time sweep at five consecutive steps (five-interval thixotropy test, 5-ITT) was performed in a controlled rate mode with changing low and high shear rates. In the recovery stage, the thixotropy

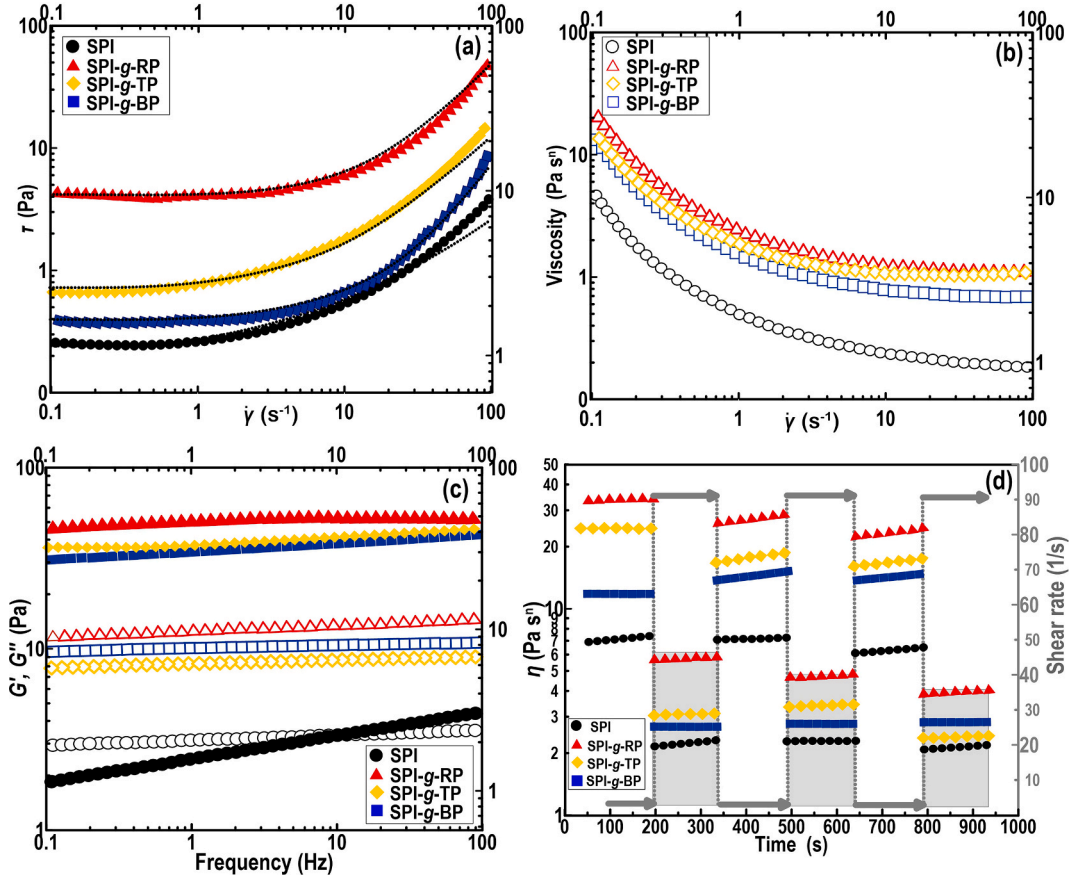

Fig. 5. (a): Shear stress-shear rate; (b): Viscosity-shear rate curves of SPI-based inks; (c): Frequency sweep curves of SPI-based inks, where G' is solid symbols and G'' is open symbols; (d): The 5-ITT of prepared Pickering emulsion variants.

of the ink is often characterized. This test is often utilized to mimic the viscosity change of the emulsion over time before (low shear), during (high shear), and after (low shear) 3D printing (Montoya et al., 2021). Remarkably, the impacts of shear rate and time on viscosity were simultaneously investigated by monitoring the emulsion system response of the 5-ITT method (Fig. 5d). When the shear rate was increased from 0.1 to 90 s^{-1}, all emulsions offered shear-sensitive features with an important reduction of viscosity. The viscosity changes at two different shear rates further verified the *pseudoplastic* feature of the emulsions (Gao et al., 2021). This shows that an arrangement structure of emulsion droplets in the ink system was broken down, resulting in a rapid reduction of viscosity, which mimicked the time of ink passing through the narrow needles of the printing systems (Li, Fan, & Li, 2023). While the emulsion structure was partially restored quite quickly once the shear rate was readjusted to the initial value (0.1 s^{-1}), demonstrating its capacity for structure recovery, simulating the emulsion adequately restored its mechanical strength upon passing through the needle to resist the repeated load of deposited layers. At this phase, the viscosity of inks would be slightly lower than that of the first stage (i.e., its initial value). In addition, the SPI–*g*–polyphenol emulsions all also showed a time-dependent behavior, in which their viscosity values increased more compared to ink prepared by neat SPI. This shows SPI–*g*–polyphenol emulsions have more resistance, as well as ability to recover from a rapid deformation than emulsions stabilized solely by neat SPI. It could be concluded that the SPI–*g*–polyphenol emulsions have rearranged under shear, and the low-speed shear would be helpful to the formation of structure of these emulsions, while the high shear would break their structure (Shahbazi et al., 2021b). To sum up, the 5-ITT established that the grafting of polyphenols onto SPI plays an influential role in the recoverability of emulsion-based ink.

3.2.3. Adsorption kinetics and structural rearrangements

The adsorption kinetics and interfacial surface pressure of printable inks at the O/W interface were evaluated to detect the emulsification mechanism of SPI-*g*-polyphenol conjugates. Fig. 6a shows the interfacial surface pressure (π) as a function of the square root of time ($t^{0.5}$) regarding control or grafted SPI-polyphenol inks at the O/W interface. In general, the dynamic adsorption feature of colloidal dispersion at the O/W interface mostly includes actual adsorption (unfolding and penetration), diffusion, and conformational reorganization (Dickinson, 2008). The adsorption kinetic is governed by the diffusion of conjugates if the plot of π versus $t^{0.5}$ is linear, and the curve of the slope signifies the diffusion rate (k_{diff}) (Zhang et al., 2021). Regarding all inks, the π was gradually increased with adsorption time, which is possibly associated with the gradual particle adsorption at the O/W interface (Perez, Carrara, Sánchez, Santiago, & Patino, 2009; Shahbazi et al., 2022b).

Besides, the Ward-Tordai equation, valid at the early stages of the diffusion-adsorption process, was used to monitor the changes of π versus adsorption time (t):

$$\pi = 2C_0 k_B T \left(Dt/3.14\right)^{0.5} \tag{5}$$

Here C_0 is the concentration of the continuous phase, k_B is the Boltzmann constant, T is the absolute temperature and Dt is the diffusion coefficient of the emulsifier at t. The diffusion rate constant (K_{diff}) is calculated as the slope of π versus $t^{0.5}$. As calculated using Eq. (5), the diffusion rate of SPI-*g*-TP, SPI-*g*-BP, and SPI-*g*-RP was 0.3125, 0.3156,

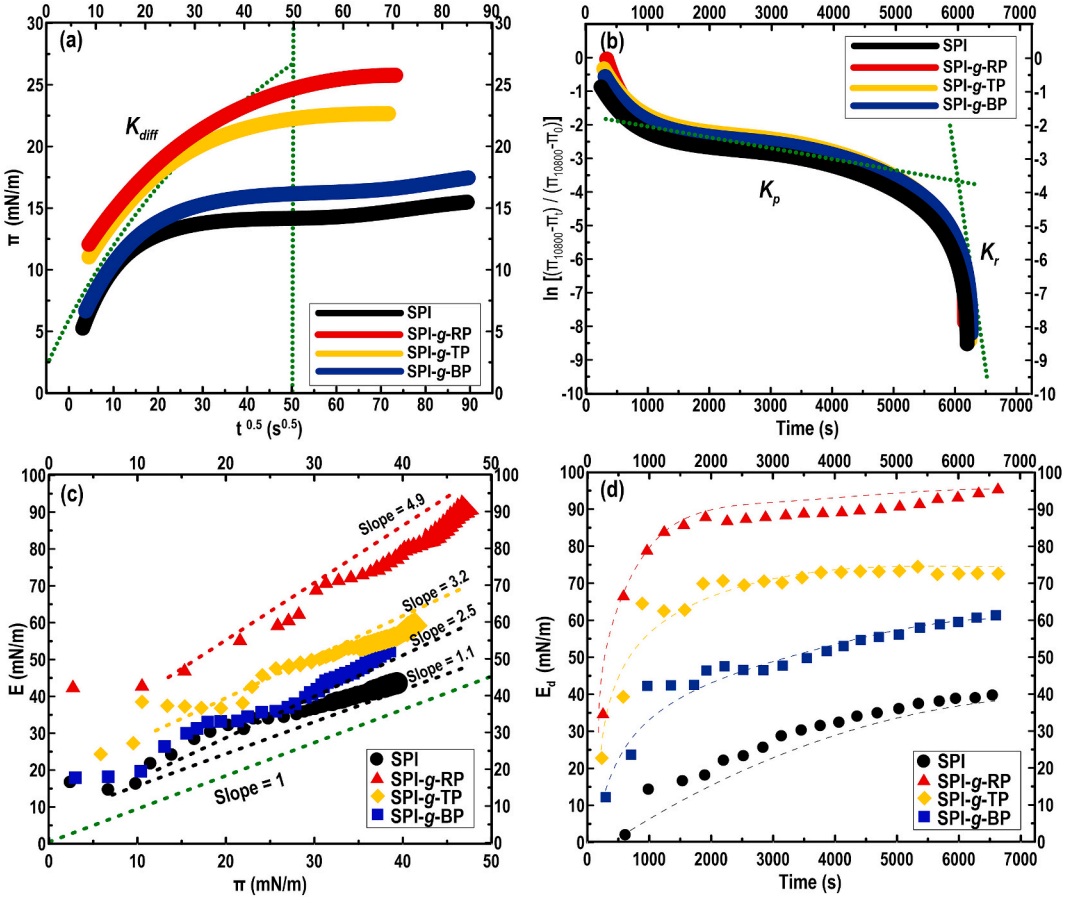

Fig. 6. (a): Time dependence of surface pressure (π) SPI-g-polyphenols adsorbed films at the O/W interface. (K_{diff}) represents diffusion rate. (b) The typical profile of the molecular penetration and configurational rearrangement steps at the O/W interface. K_p and K_r represent first-order rate constants of penetration and rearrangement, respectively. (c): Surface dilatational modulus (E) as a function of surface pressure (π); (d) Time-dependent dilatational elasticity (E_d).

and 0.3141 mN/m/s$^{0.5}$, respectively, which was basically equal to the SPI-based ink (0.3111 mN/m/s$^{0.5}$). Though, the initial surface pressures of SPI ($\pi_0 = 4.76$ mN/m) and SPI-*g*-BP ($\pi_0 = 6.39$ mN/m), and the final surface pressure (π_{10800}) after 2 h adsorption were lower than those of the SPI-*g*-TP ($\pi_0 = 10.23$ mN/m) and SPI-*g*-RP ($\pi_0 = 11.47$ mN/m). This proposes that the grafting of TP or RP polyphenol offered a desired influence on the diffusion–adsorption of SPI. Therefore, the development of aggregated networks and/or aggregated particles slows down the adsorption rate of the solid particles at the O/W interface. Furthermore, the adsorption of grafted conjugates can increase the electrostatic repulsion and steric hindrance between the oil droplets, leading to better emulsification. On the other hand, the improvement of surface hydrophobicity after grafting (Fig. 3f) was beneficial to enhance the adsorption rate of particles from the SPI-polyphenol conjugates to the O/W interface (Dickinson, 2003).

Furthermore, the rates of penetration and rearrangement of the adsorbed layer at the interface can be analyzed by the first-order equation (Ward & Tordai, 1946):

$$\ln\left[\left(\pi_f - \pi_t\right) / \left(\pi_f - \pi_0\right)\right] = -k_i t \quad (6)$$

where π_f, π_0, and π_t are the interfacial pressures at the final adsorption time, at the initial time, and at any time of each stage, respectively, and k_i is the first-order rate constant. The application of Eq. (6) to the adsorption of the biopolymer particles at the interface was presented in Fig. 6b. Clearly, there were two linear regions in these plots. Generally, the first slope is usually regarded as a first-order rate constant of penetration (K_P), while the second slope takes to a first-order rate constant of molecular reorganization (K_R) (Perez et al., 2009). Interestingly, the differences in the type of grafted SPI-polyphenols did not have any effect on the rate of penetration (K_P) and rearrangement (K_R) at the interface. Similar results were reported in the literature (Xiong, Ren, Li, & Li, 2018).

3.2.4. Dilatational rheological properties

Generally, dynamic viscoelastic features of the adsorbed layer at O/W interfaces can be used to predict ink stability (Murray, 2002). For this reason, the surface dilatational modulus (E) relates to the mechanical strength of the interfacial absorbed layer of SPI-polyphenol particles. It can be obtained from an alteration of dilatational stress (interfacial tension, γ) caused by a small change in surface area (dilatational strain) (Eggers & Villermaux, 2008). The surface dilatational modulus (E, $E = E_d + iE_v$) comprises imaginary parts (loss component, $E_v = |E| \sin\delta$) and real (storage component, $E_d = |E| \cos\delta$), where the phase angle (δ) among strain and stress can be an illustration of relative viscoelasticity of the adsorbed layer at O/W interfaces (Chang & Franses, 1995).

Fig. 6c shows the interfacial surface pressure (π)-dependence of the surface dilatational modulus (E). The E values were increased instantly due to the adsorption of particles consisting of SPI-polyphenol conjugates at the O/W interfaces, in which the slopes of E-π curves containing grafted SPI-polyphenol were higher than 1.0. This proposes a non-ideal feature for stronger interactions among these inks. However, the E-π curve slopes of the SPI-*g*-RP increased more due to higher surface hydrophobicity and greater elastic modulus of its ink constituents, which suggested that a higher content of conjugates may be needed at the O/W interface to create the required interactions between the protein particles on the surface of droplets. Compared to inks including grafted SPI-polyphenols, the E of the unmodified SPI-adsorbed layer was significantly smaller, which specified that the interaction between the SPI particles on the O/W interface was weak. This result could be associated with the higher particle size, lower surface hydrophobicity, and weaker elastic modulus of ink with SPI alone, leading to lower emulsion stability.

Besides, Fig. 6d shows the absorption time-dependence of dynamic dilatational elastic modulus (E_d) of interfacial layers. Obviously, the values of E_d were progressively increased as a result of the adsorption of SPI-polyphenol conjugates on the O/W interface with a possible formation of interactions between adsorbed particles. Yet, the inks contained grafted SPI polyphenol conjugates presented a distinctly dissimilar curve profiles compared to that of unmodified SPI. This behavior is likely associated with the adsorption and diffusion changes of the SPI before and after the grafting process. Moreover, the ink including SPI-*g*-RP conjugate rapidly attained a higher E_d values in comparison with inks with SPI-*g*-BP and SPI-*g*-TP and continued to remain largely unchanged with the adsorption time. The considerably higher surface hydrophobicity, smaller size, and mechanically stronger ink formed from SPI-*g*-RP greatly improved its adsorption, diffusion, and rearrangement to the interface.

3.3. Characterization of 3D printed structures

3.3.1. Printing quality

One of the objects of the current study was to develop printable inks, which could be printed with the appropriate printing quality, enhanced deposited layers resolution, and shape stability after printing. The inks with different types of SPI–*g*–polyphenol conjugates were printed through layer-by-layer deposition. To quantitatively evaluate the appearance of 3D printed structures the resulting images are illustrated in Fig. 7. The control ink, with unmodified SPI, spread on the bed of the 3D printer when directly deposited, indicating that in this case the layers were comparatively unsupportable. Therefore, this formulation showed a weak network system, resulting in an inferior precision shape with a low spatial resolution. Similarly, SPI-*g*-TP ink exhibited a lack of development of an appropriate geometry for the printing process. As mentioned above, SPI-*g*-TP ink has low elastic behavior with a weak thixotropic feature. This presented a produced 3D structure with an unstructured geometry-retention property. In contrast, SPI-*g*-BP and SPI-*g*-RP inks developed well-defined 3D printed objects and stable structural properties. They also were self-supporting owing to their gel-like structure and outstanding structural recovery. In these printed structures, the geometrical objects of the 3D printed samples were also suitably preserved with no apparent cracking and distortion. Compared to 3D-printed SPI-*g*-BP objects, the printed SPI-*g*-RP offered better dimensional stability and printing quality. This resulted in the 3D printed SPI-*g*-RP showing the necessary durability in supporting the deposited layers, and therefore leading to an improved shape-fidelity and resolution (Shahbazi, Jäger, Ettelaie, & Ulbrich, 2022; Shahbazi et al., 2022c).

3.3.2. Microstructural observations

The microstructural observations of 3D printed SPI-based objects without SPI-*g*-polyphenol conjugates offered non-spherical shaped coalesced pockets/pools of fat and a continuous protein phase (Fig. 7). The shape of the milk fat globules in the planted-based product is a function of the shearing during 3D printing and by coalescence of the fat globules during its processing (Grasso, Roos, Crowley, Arendt, & O'Mahony, 2021). The CLSM analysis sample containing SPI-*g*-polyphenol conjugates showed the fat globules were distributed throughout the protein network. Comparable microstructural features have been obvious from the previous works (Shahbazi et al., 2021a), where the fat globules had smooth surfaces with spherical and non-spherical shapes. Differently from the dairy products, the plant-based products showed a distribution of fat globules, which had a generally spherical shape, within a matrix of starch and other biomaterials.

3.3.3. Oral tribology properties

The oral tribological process can be considered valuable for understanding the lubrication behavior in clarifying mechanisms involved in the perception of sensory attributes elicited by printed samples, which therefore can be assigned to the satiating expectation cues (Shahbazi et al., 2021a). The Stribeck curves (log *CoF* versus log ν_s) are displayed the friction performance of the 3D printed samples as influenced by

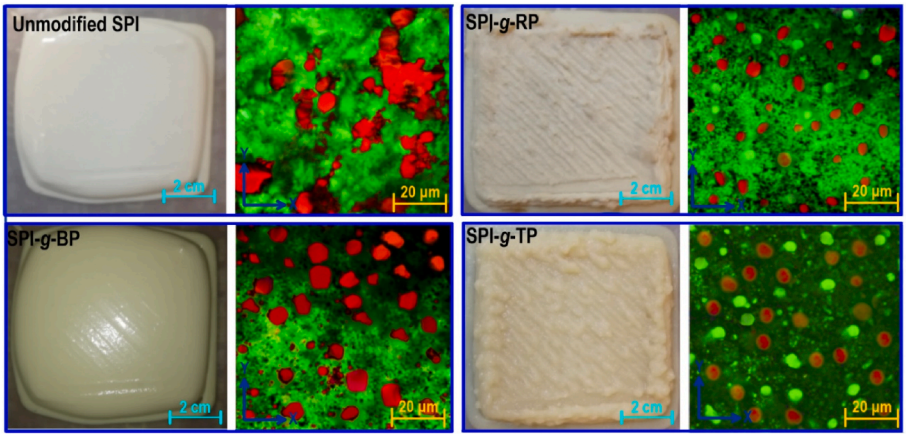

Fig. 7. Printing performance of different 3D printed objects and their relevant CLSM.

grafting treatment and saliva mixing (Fig. 8a and c). It was found that all 3D printed variants showed both boundary and mixed regimes of typical Stribeck curves. The Stribeck curve data indicated that there were some differences between 3D printed constructs in a sliding speed of <1 mm s^{-1} (Fig. 8a). This result signified that replacing oil with micro-biosurfactant did not show any obvious impact on the tribological feature at the low sliding speed range ($0.01 \leq \nu_s \leq 1$ mm s^{-1}). As the speed increased ($\nu_s \geq 1$ mm s^{-1}), the samples are entrained into the contact, creating a pressure that supports the separation of the solid surfaces, causing the decreased friction effects. Fig. 8a shows the alterations in the lubrication features among the 3D printed objects increased in the mixed regimes. Compared to printed SPI, the 3D printed SPI-*g*-TP and SPI-*g*-BP presented a significant increase in the friction effects ($p < 0.05$), while there was a considerable decrease in the *CoF* regarding printed SPI-*g*-RP ($p < 0.05$). The lower *CoF* of this printed sample can be a sign of the desired lubrication feature.

A key parameter that is often overlooked while evaluating the tribological feature of food systems is the impact of saliva on lubrication and its interaction with the food constituents. The results presented in Fig. 8b and d, revealed that the saliva-containing 3D printed samples gave much higher friction than those of free-saliva ones (Fig. 8a and c). The tribological data showed that when saliva-containing 3D printed objects were sheared between the tested hydrophobic surfaces, the *CoF* value was increased compared to corresponding printed samples without saliva. This is outstanding as saliva alone acts as an appropriate lubricant, which develops the wear-resistant film in the oral cavity via the assembly of small molecular weight proteins layer along with mucins. In this scenario, a lower *CoF* was expected through the key biological lubricant of the mouth, *i.e.*, saliva, presented in the tribological contact. Apparently, the saliva acted like a bulk protein concerning adherence and increasing the *CoF*.

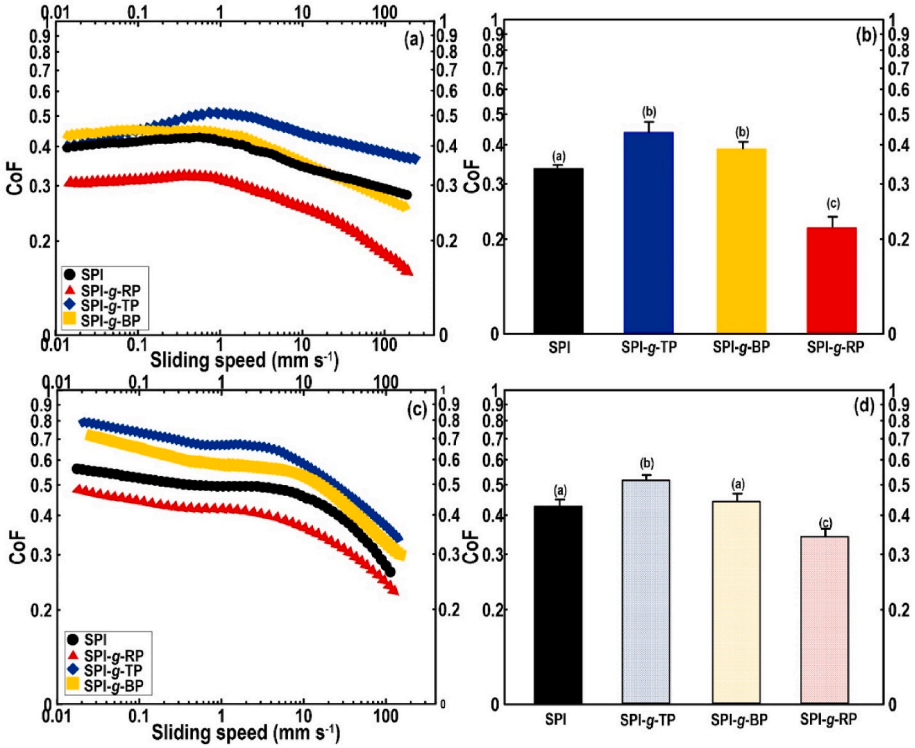

Fig. 8. The friction curves of 3D printed samples without **(a)** and with saliva **(c)**. The measured coefficient friction of printed samples without **(b)** and with saliva **(d)**. The means inside each column with different letters (a–c) are significantly different ($P < 0.05$), Duncan's test.

3.3.4. Dynamic sensory evolution

The evaluation of 3D printed cheese analogues by the temporal dominance of sensations (TDS) procedure using a trained sensory panel was suitable to provide essential information regarding the sequence of the dominant sensations in a 3D printed product once processed in the oral cavity. Fig. 9 shows the smoothed TDS curves with the related TDS significance and chance levels. Each TDS plot displays the assessed five sensory sensations of 3D printed plan-based cheeses during the standard time of 100%. In this respect, the chance level (15%) and the significance level (35%) were determined based on the binomial distribution and considering 30 observations which were afterwards plotted over the TDS curves to the assessment of the sensory data. The 3D printed SPI and SPI-*g*-TP offered a smooth sensation as dominant attributes with a max. *DR* of 71.2% and 43.8%, respectively ($P < 0.05$), in the middle of the evaluation period (Fig. 9). This was consistent with the fact that these printed samples were characterized by a weak mechanical strength and poor thixotropy behavior. In contrast, smoothness in 3D printed SPI-*g*-RP and SPI-*g*-BP were not perceived as significantly dominant at any time of evaluation ($P > 0.05$). This is possibly associated with the formation of a homogenous system with improved mechanical strength. Similarly, the firm attribute was only dominant regarding 3D printed SPI-*g*-RP and SPI-*g*-BP. By referring to previous points, the frequency sweep test of these samples was remarkably higher compared to those of SPI and SPI-*g*-TP. This presents strong 3D structural strength with a denser network structure. Concerning creaminess, the panelists could perceive the creaminess as a dominant attribute in all samples and dominated during the entire evaluation period. All printed objects including SPI-polyphenol conjugates experienced the dominance of the thick sensation. In this case, the panelist did not detect the thickness as dominant in the case of 3D printed SPI. Another promising data on the role of SPI-polyphenol conjugates in texture perception of 3D printed plant-based cheese related again to printed SPI-*g*-RP and SPI-*g*-BP, which presented a mouth-coating texture. A hypothesis to explain this phenomenon is likely that RP and BP polyphenols developed a lubricating property during mastication with the production and stabilization of the imitated cheese matrix.

4. Conclusions

An innovative antioxidative hydrophobic ink involving grafting different types of polyphenols onto SPI, was developed as a printable ink for direct-ink-write 3D food printing. The interfacial and emulsifying behavior of SPI–*g*–polyphenol inks were evaluated through multiple techniques, such as frequency sweep, interfacial shear rheology, CLSM, and physical stability experiments. It was shown that the grafting of polyphenols could notably affect the interfacial features of SPI particles. The surface and interfacial tensions were noticeably decreased with polyphenol grafting. The utilized SPI-polyphenol conjugates were moderately adsorbed at the O/W interface with quick-developing kinetics, and their interfacial moduli increased with the grafting of polyphenols. Furthermore, the grafting of polyphenols showed a strong impact on the diffusion, adsorption, and rearrangement rates of protein particles at the O/W interface, influencing the viscoelastic properties and lower surface pressure in the interface adsorption layer. These phenomena resulted in stable emulsion with small oil droplets. Thus, the SPI-polyphenol conjugates interfacial layers concerning their capacity to develop and stabilize O/W emulsion and can aid in understanding the role of interfacial rheological features in macroscopic emulsion stability. The increase in the electrostatic repulsion and steric hindrance provided by the modified SPI between the oil droplets has the effect of simplifying the compact structure. This promoted better interfacial adsorption behavior at the O/W interface, improved emulsion stability, and a

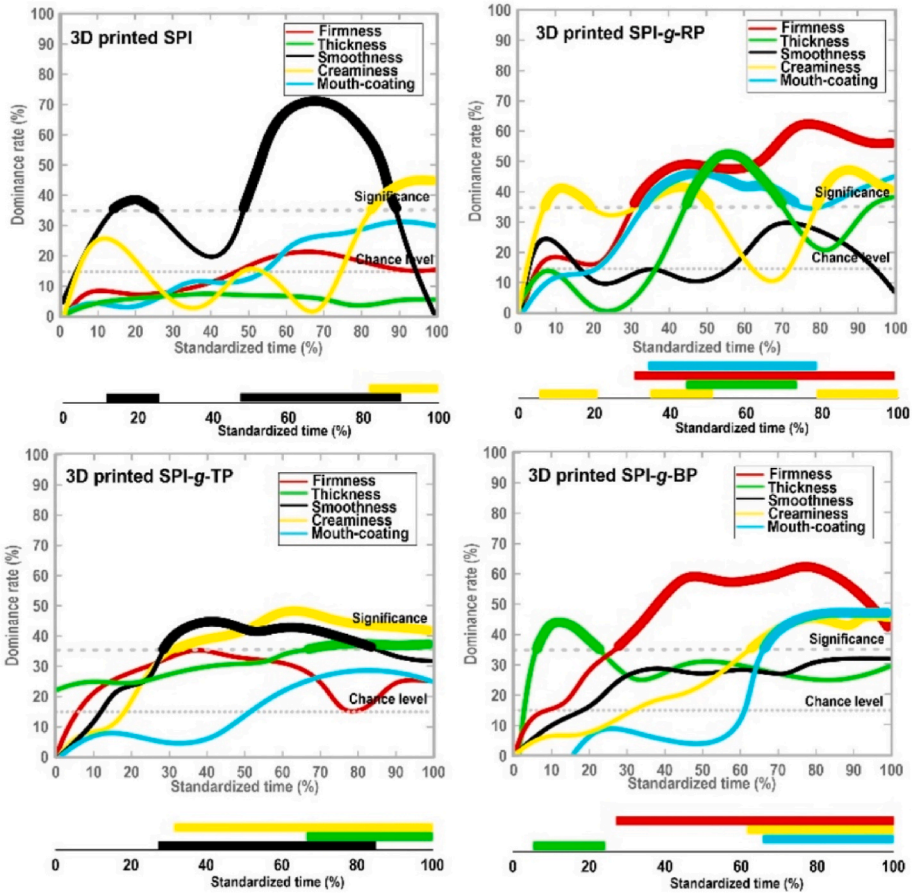

Fig. 9. Temporal profiles of dominant sensations in standardized time with defined sensations in 3D printed plant-based cheeses.

decrease in the droplet size of oils. Furthermore, thixotropy measurement showed that polyphenol grafting led to a large recovery rate of SPI emulsion-based ink, highlighting the brilliant structural recovery ability and the maintenance of structure. The 3D printing of inks containing SPI-polyphenol conjugates showed a high printing definition and shape retention, conforming to the original models. The findings of the current study can offer some novel insights for concurrently enhancing printability and self-supporting ability through the incorporation of grafted polyphenol conjugates, which can be used as a reference to develop functional antioxidative thixotropic emulsions with high potential in custom-designed distinct 3D food printing.

Funding

The research funding was provided by the University of Natural Resources and Life Sciences Vienna (BOKU).

Author statement

Adeleh Mohammadi: Methodology, Collecting data, Validation, Writing – Original draft. Peyman Asghartabar Kashi: Investigation, Collecting data, Validation. Mahboobeh Kashiri: Funding acquisition, Methodology. Amirhossein Bagheri: Methodology, Collecting data, Validation. Jianshe Chen: Methodology, Collecting data. Rammile Ettelaie: Writing – Original draft, Review & Editing. Henry Jäger: Writing – Original draft, Review & Editing, Supervision. Mahdiyar Shahbazi: Conceptualization, Methodology, investigation, Collecting data, Validation, Data interpretation, Funding acquisition, Writing – Original draft, Writing – Review & Editing.

Declaration of competing interest

The authors declare that they have no known competing financial interests or personal relationships that could have appeared to influence the work reported in this paper.

Data availability

Data will be made available on request.

Acknowledgment

The authors are grateful to Dr. Sedigheh Moghbeli from the Gorgan University of Agricultural Sciences and Natural Resources (Iran) for providing the gas chromatography results of used polyphenols in this project.

Appendix A. Supplementary data

Supplementary data to this article can be found online at https://doi.org/10.1016/j.foodhyd.2023.108851.

References

Aben, S., Holtze, C., Tadros, T., & Schurtenberger, P. (2012). Rheological investigations on the creaming of depletion-flocculated emulsions. *Langmuir, 28*, 7967–7975.

Andriamiseza, F., Bordignon, D., Payré, B., Vaysse, L., & Fitremann, J. (2022). 3D printing of biocompatible low molecular weight gels: Imbricated structures with sacrificial and persistent N-alkyl-d-galactonamides. *Journal of Colloid and Interface Science, 617*, 156–170.

Cao, Y., & Xiong, Y. L. (2015). Chlorogenic acid-mediated gel formation of oxidatively stressed myofibrillar protein. *Food Chemistry, 180*, 235–243.

Caulier, S., Doets, E., & Noort, M. (2020). An exploratory consumer study of 3D printed food perception in a real-life military setting. *Food Quality and Preference, 86*, Article 104001.

Chang, C. H., & Franses, E. I. (1995). Adsorption dynamics of surfactants at the air/water interface: A critical review of mathematical models, data, and mechanisms. *Colloids and Surfaces A: Physicochemical and Engineering Aspects, 100*, 1–45.

Chen, Q., Cao, P. F., & Advincula, R. C. (2018). Mechanically robust, ultraelastic hierarchical foam with tunable properties via 3D printing. *Advanced Functional Materials, 28*(21), Article 1800631.

Chen, Q., Chaihu, L., Yao, X., Cao, X., Bi, W., Lin, J., et al. (2021). Molecular property-tailored soy protein extraction process using a deep eutectic solvent. *ACS Sustainable Chemistry & Engineering, 9*(30), 10083–10092.

Chen, Y., Wang, Y., Yang, Q., Liao, Y., Zhu, B., Zhao, G., et al. (2018). A novel thixotropic magnesium phosphate-based bioink with excellent printability for application in 3D printing. *Journal of Materials Chemistry B, 6*, 4502–4513.

Chen, Y., Xiong, X., Liu, X., Cui, R., Wang, C., Zhao, G., et al. (2020). 3D Bioprinting of shear-thinning hybrid bioinks with excellent bioactivity derived from gellan/alginate and thixotropic magnesium phosphate-based gels. *Journal of Materials Chemistry B, 8*(25), 5500–5514.

Chen, Y., Zhang, Y., Pang, B., Liu, Z., & Liu, G. (2021). Extrusion-based 3D printing concrete with coarse aggregate: Printability and direction-dependent mechanical performance. *Construction and Building Materials, 296*, Article 123624.

Corker, A., Ng, H. C. H., Poole, R. J., & García-Tuñón, E. (2019). 3D printing with 2D colloids: Designing rheology protocols to predict 'printability'of soft-materials. *Soft Matter, 15*(6), 1444–1456.

Curcio, M., Puoci, F., Iemma, F., Parisi, O. I., Cirillo, G., Spizzirri, U. G., et al. (2009). Covalent insertion of antioxidant molecules on chitosan by a free radical grafting procedure. *Journal of Agricultural and Food Chemistry, 57*(13), 5933–5938.

Dai, S., Lian, Z., Qi, W., Chen, Y., Tong, X., Tian, T., et al. (2022). Non-covalent interaction of soy protein isolate and catechin: Mechanism and effects on protein conformation. *Food Chemistry, 384*, Article 132507.

Dickinson, E. (2003). Hydrocolloids at interfaces and the influence on the properties of dispersed systems. *Food Hydrocolloids, 17*, 25–39.

Dickinson, E. (2008). Interfacial structure and stability of food emulsions as affected by protein–polysaccharide interactions. *Soft Matter, 4*, 932–942.

Dickinson, E. (2010). Flocculation of protein-stabilized oil-in-water emulsions. *Colloids and Surfaces B: Biointerfaces, 81*, 130–140.

Dickinson, E. (2019). Strategies to control and inhibit the flocculation of protein-stabilized oil-in-water emulsions. *Food Hydrocolloids, 96*, 209–223.

Du, C., Hu, J., Wu, X., Shi, H., Yu, H. C., Qian, J., et al. (2022). 3D printing of a tough double-network hydrogel and its use as a scaffold to construct a tissue-like hydrogel composite. *Journal of Materials Chemistry B, 10*(3), 468–476.

Eggers, J., & Villermaux, E. (2008). Physics of liquid jets. *Reports on Progress in Physics, 71*, Article 036601.

Eguiluz, A., Ferrández-Montero, A., Yus, J., Sanchez-Herencia, A. J., & Ferrari, B. (2021). Dispersion of Ni nanoparticles into Ti (C, N) colloidal filaments for 3D printing by FFF. *Open Ceramics, 5*, Article 100064.

Elbadawi, M., Gustaffson, T., Gaisford, S., & Basit, A. W. (2020). 3D printing tablets: Predicting printability and drug dissolution from rheological data. *International Journal of Pharmaceutics, 590*, Article 119868.

Fahmy, A. R., Amann, L. S., Dunkel, A., Frank, O., Dawid, C., Hofmann, T., et al. (2021). Sensory design in food 3D printing–Structuring, texture modulation, taste localization, and thermal stabilization. *Innovative Food Science & Emerging Technologies, 72*, Article 102743.

Gao, Y., Lei, Y., Wu, Y., Liang, H., Li, J., Pei, Y., et al. (2021). A potential self-emulsifying agent for the construction of thermal-sensitive food W/O emulsion. *Food Chemistry, 349*, Article 129203.

Geng, M., Feng, X., Yang, H., Wu, X., Li, L., Li, Y., et al. (2022). Comparison of soy protein isolate-(–)-epigallocatechin gallate complexes prepared by mixing, chemical polymerization, and ultrasound treatment. *Ultrasonics Sonochemistry, 90*, Article 106172.

Grasso, N., Roos, Y. H., Crowley, S. V., Arendt, E. K., & O'Mahony, J. A. (2021). Composition and physicochemical properties of commercial plant-based block-style products as alternatives to cheese. *Future Foods, 4*, Article 100048.

Guinier, A. (1994). *X-ray diffraction in crystals, imperfect crystals, and amorphous bodies.* Courier Corporation.

Guo, H., Zhao, L., Qian, B., Wu, Q., Wang, R., Hua, T., … Shi, X. (2023). Direct inkjet 3D printing microwires with small feature size by freezing, sublimation, and evaporation induced colloidal nanoparticles self-assembly mechanism. *Advanced Materials Technologies, 8*(2), Article 2201132.

Gu, L., Yao, X., McClements, D. J., Liang, L., Xiong, W., Li, J., et al. (2022). Lutein-loaded emulsions stabilized by egg white protein-dextran-catechin conjugates: Cytotoxicity, stability, and bioaccessibility. *Food Biophysics*, 1–11.

Hardin, J. O., Ober, T. J., Valentine, A. D., & Lewis, J. A. (2015). Microfluidic printheads for multimaterial 3D printing of viscoelastic inks. *Advanced Materials, 27*, 3279–3284.

He, D., Xing, Y., Wang, Y., Zeng, W., Gao, W., Su, N., et al. (2022). Improved functional properties of wheat gluten hydrolysate by covalent conjugation with chlorogenic acid. *International Journal of Food Science, 58*(1), 454–462.

Hu, L., Ding, F., Liu, W., Cheng, Y., Zhu, J., Ma, L., … Wang, H. (2022). Effect of enzymatic-ultrasonic hydrolyzed chitooligosaccharide on rheology of gelatin incorporated yogurt and 3D printing. *Food Hydrocolloids, 132*, Article 107851.

Jing, Y., Diao, Y., & Yu, X. (2019). Free radical-mediated conjugation of chitosan with tannic acid: Characterization and antioxidant capacity. *Reactive and Functional Polymers, 135*, 16–22.

Kedare, S. B., & Singh, R. P. (2011). Genesis and development of DPPH method of antioxidant assay. *Journal of Food Science and Technology, 48*, 412–422.

Lee, J. H., Won, D. J., Kim, H. W., & Park, H. J. (2019). Effect of particle size on 3D printing performance of the food-ink system with cellular food materials. *Journal of Food Engineering, 256*, 1–8.

Li, X., Fan, L., & Li, J. (2023). Extrusion-based 3D printing of high internal phase emulsions stabilized by co-assembled β-cyclodextrin and chitosan. *Food Hydrocolloids, 134*, Article 108036.
Lin, Q., Chen, N., Bian, L., & Fan, M. (2012). Development and mechanism characterization of high performance soy-based bio-adhesives. *International Journal of Adhesion and Adhesives, 34*, 11–16.
Li, H., Pan, Y., Li, C., Yang, Z., Rao, J., & Chen, B. (2022). Design, synthesis and characterization of lysozyme–gentisic acid dual-functional conjugates with antibacterial/antioxidant activities. *Food Chemistry, 370*, Article 131032.
Liu, S., & Li, L. (2017). Ultrastretchable and self-healing double-network hydrogel for 3D printing and strain sensor. *ACS Applied Materials & Interfaces, 9*, 26429–26437.
Liu, X., Song, Q., Li, X., Chen, Y., Liu, C., Zhu, X., et al. (2021). Effects of different dietary polyphenols on conformational changes and functional properties of protein–polyphenol covalent complexes. *Food Chemistry, 361*, Article 130071.
Liu, F., Sun, C., Yang, W., Yuan, F., & Gao, Y. (2015). Structural characterization and functional evaluation of lactoferrin–polyphenol conjugates formed by free-radical graft copolymerization. *RSC Advances, 5*, 15641–15651.
Liu, C., Xu, N., Zong, Q., Yu, J., & Zhang, P. (2021). Hydrogel prepared by 3D printing technology and its applications in the medical field. *Colloid and Interface Science Communications, 44*, Article 100498.
Liu, Y., Zhang, W., Wang, K., Bao, Y., Regenstein, J. M., & Zhou, P. (2019). Fabrication of gel-like emulsions with whey protein isolate using microfluidization: Rheological properties and 3D printing performance. *Food and Bioprocess Technology, 12*, 1967–1979.
Li, X., Xu, X., Song, L., Bi, A., Wu, C., Ma, Y., et al. (2020). High internal phase emulsion for food-grade 3D printing materials. *ACS Applied Materials & Interfaces, 12*(40), 45493–45503.
Maldonado-Rosas, R., Tejada-Ortigoza, V., Cuan-Urquizo, E., Mendoza-Cachú, D., Morales-de La Pena, M., Alvarado-Orozco, J. M., et al. (2022). Evaluation of rheology and printability of 3D printing nutritious food with complex formulations. *Additive Manufacturing, 58*, Article 103030.
Ma, Y., Xu, D., Sang, S., Jin, Y., Xu, X., & Cui, B. (2021). Effect of superheated steam treatment on the structural and digestible properties of wheat flour. *Food Hydrocolloids, 112*, Article 106362.
McClements, D. J. (2004). *Food emulsions: Principles, practices, and techniques*. CRC press.
McClements, D. J., & Gumus, C. E. (2016). Natural emulsifiers—biosurfactants, phospholipids, biopolymers, and colloidal particles: Molecular and physicochemical basis of functional performance. *Advances in Colloid and Interface Science, 234*, 3–26.
Mishra, K., Ojha, H., & Chaudhury, N. K. (2012). Estimation of antiradical properties of antioxidants using DPPH assay: A critical review and results. *Food Chemistry, 130*(4), 1036–1043.
Mittal, A., Singh, A., Aluko, R. E., & Benjakul, S. (2021). Pacific white shrimp (Litopenaeus vannamei) shell chitosan and the conjugate with epigallocatechin gallate: Antioxidative and antimicrobial activities. *Journal of Food Biochemistry, 45*(1), Article e13569.
Mohammadi, K., Movahhedy, M. R., & Khodaygan, S. (2021). Colloidal particle reaction and aggregation control in the Electrohydrodynamic 3D printing technology. *International Journal of Mechanical Sciences, 195*, Article 106222.
Montoya, J., Medina, J., Molina, A., Gutiérrez, J., Rodríguez, B., & Marín, R. (2021). Impact of viscoelastic and structural properties from starch-mango and starch-arabinoxylans hydrocolloids in 3D food printing. *Additive Manufacturing, 39*, Article 101891.
Murray, B. S. (2002). Interfacial rheology of food emulsifiers and proteins. *Current Opinion in Colloid & Interface Science, 7*, 426–431.
Nair, S. A., Panda, S., Santhanam, M., Sant, G., & Neithalath, N. (2020). A critical examination of the influence of material characteristics and extruder geometry on 3D printing of cementitious binders. *Cement and Concrete Composites, 112*, Article 103671.
Outrequin, T. C. R., Gamonpilas, C., Siriwatwechakul, W., & Sreearunothai, P. (2022). Extrusion-based 3D printing of food biopolymers: A highlight on the important rheological parameters to reach printability. *Journal of Food Engineering*, Article 111371.
Perez, A. A., Carrara, C. R., Sánchez, C. C., Santiago, L. G., & Patino, J. M. R. (2009). Interfacial dynamic properties of whey protein concentrate/polysaccharide mixtures at neutral pH. *Food Hydrocolloids, 23*, 1253–1262.
Pineau, N., Schlich, P., Cordelle, S., Mathonnière, C., Issanchou, S., Imbert, A., … Köster, E. (2009). Temporal Dominance of Sensations: Construction of the TDS curves and comparison with time–intensity. *Food Quality and Preference, 20*(6), 450–455.
Polamaplly, P., Cheng, Y., Shi, X., Manikandan, K., Kremer, G. E., & Qin, H. (2019). 3D printing and characterization of hydroxypropyl methylcellulose and methylcellulose for biodegradable support structures. *Procedia Manufacturing, 34*, 552–559.
Qiu, R., Wang, K., Tian, H., Liu, X., Liu, G., Hu, Z., et al. (2022). Analysis on the printability and rheological characteristics of bigel inks: Potential in 3D food printing. *Food Hydrocolloids, 129*, Article 107675.
Riantiningtyas, R. R., Sager, V. F., Chow, C. Y., Thybo, C. D., Bredie, W. L., & Ahrné, L. (2021). 3D printing of a high protein yoghurt-based gel: Effect of protein enrichment and gelatine on physical and sensory properties. *Food Research International, 147*, Article 110517.
Sabet, S., Rashidinejad, A., Melton, L. D., Zujovic, Z., Akbarinejad, A., Nieuwoudt, M., et al. (2021). The interactions between the two negatively charged polysaccharides: Gum Arabic and alginate. *Food Hydrocolloids, 112*, Article 106343.
Santos, M. B., de Carvalho, M. G., & Garcia-Rojas, E. E. (2021). Carboxymethyl tara gum-lactoferrin complex coacervates as carriers for vitamin D3: Encapsulation and controlled release. *Food Hydrocolloids, 112*, Article 106347.
Shahbazi, M., & Jäger, H. (2020). Current status in the utilization of biobased polymers for 3D printing process: A systematic review of the materials, processes, and challenges. *ACS Applied Bio Materials, 4*(1), 325–369.
Shahbazi, M., Jäger, H., Chen, J., & Ettelaie, R. (2021d). Construction of 3D printed reduced-fat meat analogue by emulsion gels. Part II: Printing performance, thermal, tribological, and dynamic sensory characterization of printed objects. *Food Hydrocolloids, 121*, Article 107054.
Shahbazi, M., Jäger, H., & Ettelaie, R. (2021a). Application of Pickering emulsions in 3D printing of personalized nutrition. Part II: Functional properties of reduced-fat 3D printed cheese analogues. *Colloids and Surfaces A: Physicochemical and Engineering Aspects, 624*, Article 126760.
Shahbazi, M., Jäger, H., & Ettelaie, R. (2021b). Development of an antioxidative pickering emulsion gel through polyphenol-inspired free-radical grafting of microcrystalline cellulose for 3D food printing. *Biomacromolecules, 22*, 4592–4605.
Shahbazi, M., Jäger, H., & Ettelaie, R. (2021c). Application of Pickering emulsions in 3D printing of personalized nutrition. Part I: Development of reduced-fat printable casein-based ink. *Colloids and Surfaces A: Physicochemical and Engineering Aspects, 622*, Article 126641.
Shahbazi, M., Jäger, H., & Ettelaie, R. (2022a). A promising therapeutic soy-based pickering emulsion gel stabilized by a multifunctional microcrystalline cellulose: Application in 3D food printing. *Journal of Agricultural and Food Chemistry, 70*(7), 2374–2388.
Shahbazi, M., Jäger, H., & Ettelaie, R. (2022b). Dual-grafting of microcrystalline cellulose by tea polyphenols and cationic ε-polylysine to tailor a structured antimicrobial soy-based emulsion for 3D printing. *ACS Applied Materials & Interfaces, 14*(18), 21392–21405.
Shahbazi, M., Jäger, H., & Ettelaie, R. (2022c). Kinetic evaluation of the starch molecular behavior under extrusion-based or laser powder bed fusion 3D printing systems: A systematic structural and biological comparison. *Additive Manufacturing, 57*, 102934.
Shahbazi, M., Jäger, H., Ettelaie, R., & Chen, J. (2021e). Construction of 3D printed reduced-fat meat analogue by emulsion gels. Part I: Flow behavior, thixotropic feature, and network structure of soy protein-based inks. *Food Hydrocolloids, 120*, Article 106967.
Shahbazi, M., Jäger, H., Ettelaie, R., Mohammadi, A., & Kashi, P. A. (2023). Multimaterial 3D printing of self-assembling smart thermo-responsive polymers into 4D hierarchical mesostructured architectures: A review. *Additive Manufacturing.* , Article 103598. https://doi.org/10.1016/j.addma.2023.103598
Shahbazi, M., Jäger, H., Ettelaie, R., & Ulbrich, M. (2022d). Insights into the supramolecular structure and degradation mechanisms of starch from different botanical sources as affected by extrusion-based 3D printing. *Biomacromolecules, 24*(1), 69–85.
Sheikhi, M., Rafiemanzelat, F., Ghodsi, S., Moroni, L., & Setayeshmehr, M. (2022). 3D printing of jammed self-supporting microgels with alternative mechanism for shape fidelity, crosslinking and conductivity. *Additive Manufacturing, 58*, Article 102997.
Shi, Y., Zhang, M., & Bhandari, B. (2021). Effect of addition of beeswax based oleogel on 3D printing of potato starch-protein system. *Food Structure, 27*, Article 100176.
Sommer, M. R., Alison, L., Minas, C., Tervoort, E., Rühs, P. A., & Studart, A. R. (2017). 3D printing of concentrated emulsions into multiphase biocompatible soft materials. *Soft Matter, 13*(9), 1794–1803.
Sui, X., Sun, H., Qi, B., Zhang, M., Li, Y., & Jiang, L. (2018). Functional and conformational changes to soy proteins accompanying anthocyanins: Focus on covalent and non-covalent interactions. *Food Chemistry, 245*, 871–878.
Vadodaria, S. S., He, Y., Mills, T., & Wildman, R. (2020). Fabrication of surfactant-polyelectrolyte complex using valvejet 3D printing-aided colloidal self assembly. *Colloids and Surfaces A: Physicochemical and Engineering Aspects, 600*, Article 124914.
Wan, Y., Wang, R., Feng, W., Chen, Z., & Wang, T. (2021). High internal phase Pickering emulsions stabilized by co-assembled rice proteins and carboxymethyl cellulose for food-grade 3D printing. *Carbohydrate Polymers, 273*, Article 118586.
Ward, A. F. H., & Tordai, L. (1946). Time-dependence of boundary tensions of solutions I. The role of diffusion in time-effects. *The Journal of Chemical Physics, 14*, 453–461.
Wu, H., Cheng, Y., Liu, W., He, R., Zhou, M., Wu, S., et al. (2016). Effect of the particle size and the debinding process on the density of alumina ceramics fabricated by 3D printing based on stereolithography. *Ceramics International, 42*(15), 17290–17294.
Xiong, W., Ren, C., Li, J., & Li, B. (2018). Characterization and interfacial rheological properties of nanoparticles prepared by heat treatment of ovalbumin-carboxymethylcellulose complexes. *Food Hydrocolloids, 82*, 355–362.
Xu, Y., Han, Y., Chen, M., Luo, J., Shi, S. Q., Li, J., et al. (2021). Constructing a triple network structure to prepare strong, tough, and mildew resistant soy protein adhesive. *Composites Part B: Engineering, 211*, Article 108677.
Yan, S., Xu, J., Zhang, S., & Li, Y. (2021). Effects of flexibility and surface hydrophobicity on emulsifying properties: Ultrasound-treated soybean protein isolate. *Lwt, 142*, Article 110881.
Yan, S., Yao, Y., Xie, X., Zhang, S., Huang, Y., Zhu, H., et al. (2022). Comparison of the physical stabilities and oxidation of lipids and proteins in natural and polyphenol-modified soybean protein isolate-stabilized emulsions. *Food Research International, 162*, Article 112066.
Ye, J., Fan, F., Xu, X., & Liang, Y. (2013). Interactions of black and green tea polyphenols with whole milk. *Food Research International, 53*(1), 449–455.

Yuan, R., Wu, K., & Fu, Q. (2022). 3D printing of all-regenerated cellulose material with truly 3D configuration: The critical role of cellulose microfiber. *Carbohydrate Polymers, 294*, Article 119784.
Zeng, X., Li, T., Zhu, J., Chen, L., & Zheng, B. (2021). Printability improvement of rice starch gel via catechin and procyanidin in hot extrusion 3D printing. *Food Hydrocolloids, 121*, Article 106997.
Zhang, X., Qi, B., Xie, F., Hu, M., Sun, Y., Han, L., et al. (2021). Emulsion stability and dilatational rheological properties of soy/whey protein isolate complexes at the oil-water interface: Influence of pH. *Food Hydrocolloids, 113*, Article 106391.
Zhou, S. D., Huang, L., Meng, L., Lin, Y. F., Xu, X., & Dong, M. S. (2020). Soy protein isolate-(-)-epigallocatechin gallate conjugate: Covalent binding sites identification and IgE binding ability evaluation. *Food Chemistry, 333*, Article 127400.